UNIVERSIDAD DE GUANAJUATO

CAMPUS IRAPUATO - SALAMANCA
DIVISIÓN DE INGENIERÍAS

"LASER BEAM CHARACTERIZATION BY KNIFE-EDGE TECHNIQUE FOR HIGH-PRECISION NONLINEAR OPTICS MEASUREMENTS"

TESIS PROFESIONAL

QUE PARA OBTENER EL GRADO DE:

MAESTRO EN INGENIERÍA ELÉCTRICA

PRESENTA:

ING. LUIS DAVID LOPEZ ZAVALA

DIRECTORES:

DR. JOSÉ AMPARO ANDRADE LUCIO
DR. OLEKSIY V. SHULIKA
DR. VOLODYMYR FESENKO

SALAMANCA, GUANAJUATO DICIEMBRE 2025

UNIVERSIDAD DE GUANAJUATO

CAMPUS IRAPUATO-SALAMANCA

DIVISION DE INGENIERÍAS

Laser beam characterization by knife-edge technique for high-precision nonlinear optics measurements

MASTER THESIS

submitted in partial fulfillment of the requirements for the degree of
Master's in Electrical Engineering

BY

Luis David LOPEZ ZAVALA

Reviewers:
Dr. José Amparo ANDRADE LUCIO
Dr. Volodymyr I. FESENKO

Supervisor:
Dr. Oleksiy V. SHULIKA

Cuerpo Académico "Fotónica No Lineal"

SALAMANCA 2025

Declaration of Authorship

I, Luis David LOPEZ ZAVALA, declare that this thesis titled, "Laser beam characterization by knife-edge technique for high-precision nonlinear optics measurements" and the work presented in it are my own. I confirm that:

- This work was done wholly or mainly while in candidature for a research degree at this University.
- Where any part of this thesis has previously been submitted for a degree or any other qualification at this University or any other institution, this has been clearly stated.
- Where I have consulted the published work of others, this is always clearly attributed.
- Where I have quoted from the work of others, the source is always given. With the exception of such quotations, this thesis is entirely my own work.
- I have acknowledged all main sources of help.
- Where the thesis is based on work done by myself jointly with others, I have made clear exactly what was done by others and what I have contributed myself.

Signed: _____

Date: _____

"Talent withers where pettiness flourishes."

— Maxim Gorky.

Abstract

UNIVERSIDAD DE GUANAJUATO

Campus Irapuato-Salamanca
Division de Ingenierías

Master's in Electrical Engineering

LASER BEAM CHARACTERIZATION BY KNIFE-EDGE TECHNIQUE FOR HIGH-PRECISION NONLINEAR OPTICS MEASUREMENTS

by Luis David LOPEZ ZAVALA

Accurate characterization of laser beam profiles is essential in nonlinear optics, where key quantities such as the nonlinear refractive index n_2 and the third-order susceptibility $\chi^{(3)}$ depend sensitively on the on-axis intensity I_0, which scales quadratically with the beam waist w_0. Small uncertainties in w_0 therefore propagate into significant errors in nonlinear parameters. To address this challenge, this work develops and validates a fully automated knife-edge system for high-precision beam characterization using a 543.5 nm, 1.5 mW He-Ne laser.

The setup combines a motorized translation stage and a Thorlabs PM100D power meter controlled through a MATLAB interface that performs synchronized acquisition and robust nonlinear least-squares fitting. Each transverse scan yields the beam radius $w(z)$, beam center $r_0(z)$, and transmitted power $P_0(z)$; the waist w_0 and Rayleigh range z_R are subsequently obtained from Gaussian-propagation fits. The method was evaluated under controlled perturbations, including knife-edge rotation and deliberate beam misalignment. The beam-center trajectories $r_0(z)$ consistently revealed a small nonlinear curvature identified as an intrinsic mechanical signature of the translation platform. In contrast, the beam radius $w(z)$ remained highly stable. Using this framework, the focused-beam waist was estimated as $w_0 = 45\,\mu$m with a near diffraction-limited quality factor $M^2 = 1.17$.

Attempts to measure third-order nonlinear refraction via the Z-scan technique on $BaTiO_3$, SBN:61 ($Sr_{0.61}Ba_{0.39}Nb_2O_6$), and gel films incorporating *Hibiscus sabdariffa* extract produced no reproducible signals. This outcome is attributed to the weak intrinsic $\chi^{(3)}$ of these materials under continuous-wave excitation, the low incident power, and the millimeter-scale sample thickness, which suppress the nonlinear phase shift below the detection threshold. Despite the absence of measurable nonlinear refraction, this work demonstrates a robust and reproducible knife-edge methodology and introduces quantitative alignment metrics capable of supporting future nonlinear-optics experiments once suitable materials and excitation conditions are available.

Keywords: GAUSSIAN BEAM CHARACTERIZATION, KNIFE-EDGE TECHNIQUE, LASER PROFILING, NONLINEAR LEAST-SQUARES FITTING, NONLINEAR OPTICS CHARACTERIZATION

Resumen

UNIVERSIDAD DE GUANAJUATO

Campus Irapuato-Salamanca
Division de Ingenierías

Maestro en Ingeniería Eléctrica

CARACTERIZACIÓN DE HACES LÁSER MEDIANTE LA TÉCNICA DE LA NAVAJA PARA MEDICIONES DE ÓPTICA NO LINEAL DE ALTA PRECISIÓN.

por Luis David LOPEZ ZAVALA

La caracterización precisa del perfil e intensidad de un haz láser es fundamental en óptica no lineal, ya que parámetros como el índice de refracción no lineal n_2 y la susceptibilidad de tercer orden $\chi^{(3)}$ dependen críticamente de la intensidad en el eje I_0, la cual escala cuadráticamente con la cintura del haz w_0. Por lo tanto, pequeñas incertidumbres en w_0 pueden generar errores significativos en la estimación de parámetros no lineales. En este trabajo se desarrolla y valida un sistema totalmente automatizado para la caracterización de haces mediante la técnica de la navaja, utilizando un láser He-Ne de 543.5 nm y 1.5 mW.

El sistema integra una plataforma de traslación motorizada y un medidor de potencia Thorlabs PM100D, ambos controlados mediante una interfaz desarrollada en MATLAB que permite la adquisición sincronizada y el ajuste robusto por mínimos cuadrados no lineales. Cada corte transversal proporciona el radio del haz $w(z)$, la posición del centro $r_0(z)$ y la potencia transmitida $P_0(z)$; posteriormente, la cintura w_0 y el rango de Rayleigh z_R se obtienen mediante un ajuste a la ley de propagación gaussiana. El método se evaluó bajo perturbaciones controladas, incluyendo rotación de la navaja y desalineamientos deliberados del haz. Las trayectorias del centro del haz $r_0(z)$ revelaron de manera consistente una ligera curvatura no lineal asociada a la firma mecánica intrínseca de la plataforma de traslación. En contraste, el radio del haz $w(z)$ se mantuvo notablemente estable. Con este procedimiento se estimó una cintura enfocada de $w_0 = 45\,\mu$m, con un factor de calidad $M^2 = 1.17$ cercano al límite de difracción.

Los intentos por medir refracción no lineal de tercer orden mediante la técnica Z-scan en $BaTiO_3$, SBN:61 ($Sr_{0.61}Ba_{0.39}Nb_2O_6$) y películas de gelatina con extracto de *Hibiscus sabdariffa* no mostraron señales reproducibles. Este resultado se atribuye a la débil $\chi^{(3)}$ intrínseca de estos materiales bajo excitación continua, a la baja potencia incidente y al espesor milimétrico de las muestras, factores que reducen la fase no lineal por debajo del umbral de detección. A pesar de la ausencia de efectos no lineales medibles, este trabajo demuestra una metodología automatizada, robusta y reproducible basada en la técnica de la navaja, e introduce métricas cuantitativas de alineación capaces de servir como herramienta diagnóstica en futuros experimentos de óptica no lineal bajo condiciones de excitación adecuadas.

Palabras clave: CARACTERIZACIÓN DE HACES GAUSSIANOS, TÉCNICA DE LA NAVAJA, PERFILADO LÁSER, AJUSTE NO LINEAL POR MÍNIMOS CUADRADOS, ÓPTICA NO LINEAL

Contents

List of Figures

List of Tables

List of Abbreviations

CV	**C**oefficient of **V**ariation
GUI	**G**raphical **U**ser **I**nterface
KET	**K**nife-**E**dge **T**echnique
MAE	**M**ean **A**bsolute **E**rror
MKS	**M**etre **K**ilogram **S**econd (SI system of units)
NLA	**N**onlinear **A**bsorption
NLO	**N**onlinear **O**ptics
NLR	**N**onlinear **R**efractive index
RMSE	**R**oot **M**ean **S**quare **E**rror
R^2	**C**oefficient of **D**etermination
RWA	**R**otating **W**ave **A**pproximation
SD	**S**tandard **D**eviation
SNR	**S**ignal-to-**N**oise **R**atio
SHG	**S**econd **H**armonic **G**eneration
SPM	**S**elf **P**hase **M**odulation
SVEA	**S**lowly **V**arying **E**nvelope **A**pproximation
TEM00	**T**ransverse **E**lectromagnetic Mode **00**
THG	**T**hird **H**armonic **G**eneration

Physical Constants

Pi	$\pi = 3.141\,592\,653\,59$
Speed of Light	$c_0 = 2.997\,924\,58 \times 10^{8}\,\mathrm{m\,s^{-1}}$
Vacuum electric permittivity	$\epsilon_0 = 8.854\,187\,81 \times 10^{-12}\,\mathrm{F\,m^{-1}}$
Vacuum magnetic permeability	$\mu_0 = 12.566\,370\,614\,4 \times 10^{-7}\,\mathrm{H\,m^{-1}}$

List of Symbols

α_0	linear absorption coefficient	m^{-1}
χ	optical susceptibility	
$r_0(z)$	beam center position along z	m
$w(z)$	beam radius at position z	m
w_0	beam waist (minimum radius)	m
z_0	waist location along propagation axis	m
z_R	Rayleigh range	m
θ_0	divergence half–angle	rad
M^2	beam quality factor	–
f	focal length of lens	m
d	beam diameter before lens	m
P_0	maximum transmitted power	W
I_0	on-axis intensity	$\mathrm{W/m^2}$
σ_{r_0}	standard deviation of $r_0(z)$	m
$\frac{dr_0}{dz}$	slope of beam-center trajectory	$\mathrm{m\,m^{-1}}$
Δy_{10-90}	10–90% knife-edge width	m
erf	error function	–
erfc	complementary error function	–
n_2	nonlinear refractive index	

Dedicated to those whose presence was truly constructive.

Chapter 1

Introduction

The study of light–matter interaction has been a central topic in physics since the origins of optics. From the classical formulations of reflection and refraction to the development of electromagnetic theory and quantum mechanics, each step in our understanding of light has revealed new ways to control and exploit its properties. The advent of the laser in the 1960s represented a turning point by enabling the production of coherent, monochromatic, and highly intense radiation, thus opening the door to a new domain: nonlinear optics. These phenomena arise when the polarization response of a material ceases to be proportional to the applied electric field. Under these conditions, the superposition principle is no longer valid, and light can interact with itself through the medium, giving rise to effects such as harmonic generation, self-focusing, and intensity-dependent refractive index changes. These phenomena are not only of fundamental scientific interest but also essential to modern technologies such as ultrafast spectroscopy, optical communications, and laser–matter processing. Accurate characterization of the spatial and intensity distribution of laser beams is therefore a prerequisite for the reliable measurement of nonlinear optical coefficients, such as the nonlinear refractive index n_2 and the third-order susceptibility $\chi^{(3)}$. Among the experimental techniques available for beam characterization, the knife-edge technique stands out for its simplicity, robustness, and direct connection to the Gaussian beam model. However, despite its conceptual simplicity, obtaining consistent and reproducible results requires precise alignment, automated control, and careful numerical treatment of the acquired data.

The present work is motivated by this need for precision and reproducibility in beam characterization for nonlinear optical measurements. It focuses on the development of an automated knife-edge system capable of scanning, acquiring, and processing the transmitted power with high spatial resolution. The system integrates a translation stage, optical power meters, and a MATLAB-based interface that performs nonlinear fitting, alignment diagnostics, and beam waist reconstruction. The extracted parameters: beam waist w_0, Rayleigh range z_R, and waist position z_0, are used to quantify the optical field distribution and to evaluate alignment stability.

Finally, the results are discussed in the broader context of nonlinear optics. By establishing a reliable experimental foundation for beam waist determination, this work contributes to the accurate estimation of n_2 and $\chi^{(3)}$, parameters that ultimately define the nonlinear response of materials. In this way, the thesis bridges the gap between optical instrumentation, data analysis, and the characterization of nonlinear optical phenomena, forming a complete and reproducible workflow for experimental photonics research.

Chapter 2

Gaussian Beam

In physics, light is described as an electromagnetic wave that propagates in free space at the constant speed c. The electric field distribution can be represented by a field that satisfies the wave equation, a second-order partial differential equation which describes the propagation of a disturbance, such as an electromagnetic field, in space and time. Under the assumption of harmonic time dependence, the wave equation reduces to the Helmholtz equation, which serves as the starting point for the analysis of laser beam propagation in homogeneous media:

$$\nabla^2\psi + k^2\psi = 0, \tag{2.1}$$

where $\nabla^2 = \frac{\partial^2}{\partial x^2} + \frac{\partial^2}{\partial y^2}$ is the transverse Laplacian operator, and $k = 2\pi/\lambda = \omega/c$ is the wave number. Any function that satisfies Eq. 2.1 represents a possible spatial distribution of an optical field under stationary conditions [1], [2]. In the context of laser optics, a basic class of solutions to the Helmholtz equation are monochromatic waves with harmonic time dependence, typically expressed as

$$\psi(\mathbf{r}, t) = \psi(\mathbf{r})e^{-i\omega t},$$

with $\mathbf{r} = (x, y, z)$ denotes the position vector. Among these, paraxial waves are of particular importance in laser applications, as they describe beams propagating at small angles with respect to the optical axis. The most relevant solution under this approximation is the *Gaussian beam*, whose fundamental mode exhibits a characteristic transverse confinement and well-defined phase structure [1], [3]. Rather than introducing its analytical form at this stage, it is convenient to note that the Gaussian beam arises naturally as a solution to the paraxial Helmholtz equation when the optical field is described through a slowly varying complex envelope. Its amplitude, phase curvature, and Gouy phase all result from this approximation, as shown below. To obtain it, we represent a monochromatic field as

$$\psi(\mathbf{r}) = A(\mathbf{r})e^{-ikz},$$

where $A(\mathbf{r})$ is a slowly varying complex envelope. Substituting this form into the Helmholtz equation 2.1 and neglecting the second derivative $\partial^2 A/\partial z^2 \ll k\,\partial A/\partial z$ leads to the paraxial Helmholtz equation:

$$\nabla_\perp^2 A - i\,2k\,\frac{\partial A}{\partial z} = 0, \tag{2.2}$$

with $\nabla_\perp^2 = \partial^2/\partial x^2 + \partial^2/\partial y^2$ the transverse Laplacian.

2.1 Gaussian beam solution

A fundamental class of solutions to Eq. (2.2) is obtained by introducing the complex beam parameter

$$q(z) = z + iz_0,$$

where z_0 is the Rayleigh range. Writing

$$\frac{1}{q(z)} = \frac{1}{R(z)} - i\,\frac{\lambda}{\pi w^2(z)},$$

allows the field to be expressed as

$$\psi(x,y,z) = A_0 \frac{w_0}{w(z)} \exp\left[-\frac{x^2+y^2}{w^2(z)}\right] \exp\left(-ikz - i\frac{k(x^2+y^2)}{2R(z)} + i\zeta(z)\right), \tag{2.3}$$

The additional phase term $\zeta(z)$ is the Gouy phase, representing a π phase shift accumulated through the focus. Equations (2.3)–(2.2) form the complete paraxial description of the fundamental Gaussian mode, which underpins the knife-edge beam characterization used in this work. Although Gaussian beams are not exact solutions of Maxwell's equations, they provide an excellent approximation whenever the waist is much larger than the wavelength or, equivalently, when the divergence is small. Their systematic study began shortly after the invention of the laser, particularly through the seminal work of Kogelnik and Li [4] and early analyses by Goubau [5]. Since then, Gaussian beams have been recognized as fundamental optical modes. Moreover, more complex electromagnetic fields are often expressed as superpositions of Gaussian modes, reinforcing their role as the building blocks of modern laser optics [3], [6], [7]. The full derivation of the Gaussian beam solution involves assuming a separable ansatz for the envelope $A(x,y,z)$, applying the method of complex beam parameters, and enforcing consistency between the transverse Laplacian and the longitudinal evolution. Since this procedure is standard and extensively documented [1], [2], only the resulting expressions are presented here.

2.2 Characteristics of a Gaussian Beam

The importance of these modes becomes evident when considering the fundamental transverse electromagnetic mode (TEM_{00}), which is the natural operating state of most lasers. In this case, the beam intensity follows an approximately Gaussian distribution across the transverse plane. An ideal Gaussian beam exhibits a maximum intensity at the optical axis ($r = 0$), decreasing monotonically toward the edges according to an exponential law. Mathematically, the transverse intensity $I(r)$ is expressed as [1], [2]:

$$I(r) = I_0 \exp\left(-\frac{2r^2}{w^2}\right),$$

where I_0 is the maximum intensity at the beam center, and w is the beam radius at the considered cross-section. By definition, the radius w is taken as the distance from

the central axis to the point where the intensity drops to $1/e^2 \approx 13.5\%$ of I_0. That is, at $r = w$ one has $I(w) = I_0/e^2$. This convention implies that most of the optical power (about 86.5%) is contained within the circle of radius w. The beam diameter is then usually defined as $D = 2w$ [8]. An important feature of the Gaussian beam is that its profile remains Gaussian along propagation, although the parameter beam width $w(z)$ varies with distance z. There exists a particular point, called the beam waist, where the radius $w(z)$ reaches its minimum value, denoted w_0. At the waist the beam is most concentrated. At larger distances, the beam expands due to diffraction: the radius $w(z)$ grows hyperbolically with z. The exact dependence is given by the classical Gaussian beam expression [1], [2], [3]:

$$w(z) = w_0 \sqrt{1 + \left(\frac{z - z_0}{z_R}\right)^2}, \tag{2.4}$$

where z_0 is the axial position of the waist and z_R is the Rayleigh range. The Rayleigh range z_R is defined as the distance from the waist to the point where the beam cross-sectional area doubles to $w = \sqrt{2}\, w_0$. In the case of a monochromatic beam with wavelength λ in free space, z_R is given by [1]:

$$z_R = \frac{\pi w_0^2}{\lambda},$$

This parameter characterizes the depth of focus of the beam: essentially, it determines the region around the waist in which the beam remains approximately constant in size before starting to diverge significantly. For $z \gg z_R$, the divergence approaches the asymptotic value $\Theta_0 \approx \lambda/(\pi w_0)$. Figure 2.1 illustrates this hyperbolic evolution of the beam radius, showing how the waist determines the far-field divergence. The phase of the Gaussian beam also evolves during propagation. While the wavefront is planar at the waist, it gradually acquires curvature described by

$$R(z) = z \left[1 + \left(\frac{z_R}{z}\right)^2\right], \tag{2.5}$$

so that $R(z) \to \infty$ at the waist and $R(z) \approx z$ far from it, corresponding to a spherical phase front [1]. Additionally, the beam undergoes a longitudinal phase anomaly known as the Gouy phase shift,

$$\zeta(z) = \arctan\left(\frac{z}{z_R}\right), \tag{2.6}$$

which introduces an extra phase of π as the beam propagates from $-\infty$ to $+\infty$. This effect, absent in plane waves, plays a key role in interferometry and nonlinear optics [2]. Together, these parameters provide a complete description of the Gaussian beam: its confinement near the waist, the divergence dictated by diffraction-limited propagation, the curvature of its phase fronts, and the unique phase evolution associated with the Gouy shift [1], [2], [8].

In the formulas above, it was assumed that the waist position z_0 is at $z = 0$. For the general case, z must be replaced by $z \to z - z_0$ [8]. Thus a Gaussian beam is completely described by its waist w_0 and its position, from which all other parameters can be derived. Its transverse intensity follows a quadratic exponential profile and presents

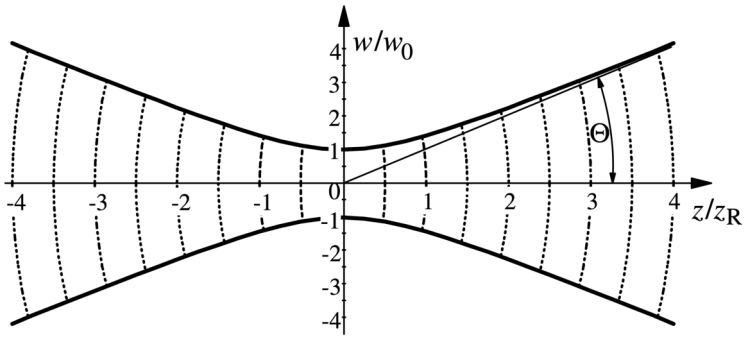

FIGURE 2.1: Evolution of the beam radius $w(z)$ relative to the waist w_0 as a function of the normalized distance z/z_R. Source: [8].

wavefronts of increasing curvature as it propagates away from the waist. Moreover, it is stable under paraxial propagation: it preserves its Gaussian functional form, only with a variable width $w(z)$. These properties make the Gaussian beam a particularly useful solution to describe the propagation of laser light [1], [2], [3], [8].

2.3 Gaussian beam power distribution

The total optical power carried by the beam at a given axial position z is obtained by integrating the intensity (Eq. 3.1) over the transverse plane. Using polar coordinates, this yields

$$P(z) = \int_0^{2\pi} \int_0^{\infty} I(r)\, r\, dr\, d\theta = \frac{\pi}{2}\, w^2(z)\, I_0, \tag{2.7}$$

which shows that the total power remains constant: as $w(z)$ increases due to diffraction, the peak intensity I_0 decreases accordingly, conserving energy flux. This expression is also useful for calculating the power fraction transmitted through apertures or partially obstructed by knife-edges, which will be employed in subsequent sections for beam profiling analysis.

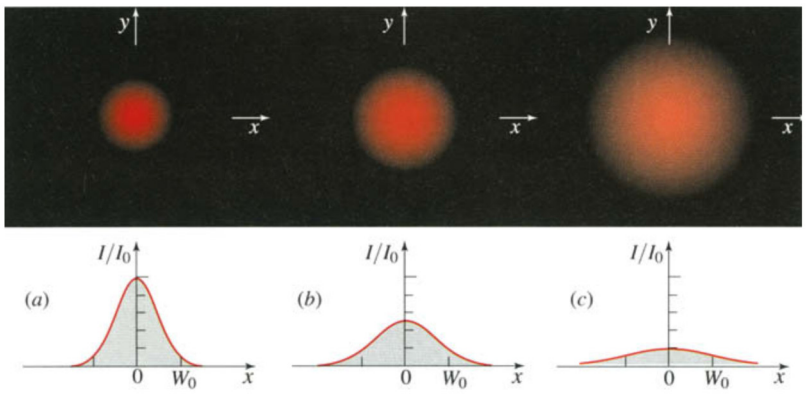

FIGURE 2.2: Normalized transverse intensity profiles $I(r)/I_0$ at various axial positions: (a) $z = 0$, (b) $z = z_R$, and (c) $z = 2z_R$. Source: [1].

Figure 2.2 illustrates the evolution of the normalized transverse intensity as the beam propagates from the waist ($z = 0$) through the Rayleigh range ($z = z_R$) and beyond. As expected, the beam broadens and the peak intensity diminishes due to diffraction, while the total power remains constant. Understanding this distribution is particularly important because it provides a measurable signature of the beam's geometry and propagation characteristics. Although the Gaussian beam is the most commonly used model, other solutions exist for particular boundary conditions, including higher-order Hermite–Gaussian and Laguerre–Gaussian modes [2]. In this work, however, we restrict our attention to the fundamental Gaussian mode, which accurately describes tightly focused laser beams under typical laboratory conditions. Accurate knowledge of the beam waist, divergence, and related parameters is essential in a wide range of optical applications, including Z-scan measurements, fiber coupling, and nonlinear spectroscopy [9]. Since these quantities cannot be accessed directly, they must be inferred from spatial intensity data using appropriate diagnostic techniques. Among these, the *knife-edge method* stands out for its simplicity, robustness, and sub-millimeter spatial precision. The following chapter provides an overview of this technique and its relevance for Gaussian beam characterization.

Chapter 3

Knife-edge Technique Fundamentals

Several techniques have been developed for laser beam profiling, such as the slit-scan method [10], [11] and the pinhole technique [12]. Nevertheless, one of the most widely adopted approaches is the knife-edge method [13], [14]. The knife-edge technique is a well-established method for determining the transverse profile of laser beams, particularly useful when Gaussian behavior is expected. Its simplicity and high spatial resolution make it ideal for characterizing tightly focused beams, where camera-based methods may suffer from limitations in resolution, alignment, or sensitivity [13], [14]. Moreover, it provides a fast and cost-effective way to obtain accurate estimates of fundamental beam parameters, which explains its extensive use in both research and industrial applications. The intensity distribution of the fundamental transverse mode of a Gaussian laser beam satisfaces the equation:

$$I(x,y) = I_0 \exp\left(-\frac{2(x^2+y^2)}{w^2(z)}\right), \tag{3.1}$$

where $I(x,y)$ is the optical intensity at the point (x,y), I_0 represents the peak intensity at the beam center, and $w(z)$ is the beam radius at the longitudinal position z. The latter is defined as the radial distance from the beam axis at which the intensity decreases to $1/e^2$ of its maximum value [12], [13], [15], [16]. The total power of the beam at a fixed longitudinal position z is obtained by integrating the intensity distribution in Eq. (3.1) over the entire transverse plane:

$$P_0 = \iint_{-\infty}^{\infty} I(x,y)\,dx\,dy = I_0 \frac{\pi w^2(z)}{2}, \tag{3.2}$$

as shown in the previous chapter 2.3. This result expresses the conservation of the optical power carried by the Gaussian mode. When a knife-edge partially blocks the beam along one transverse direction, the integration limits are modified, and the resulting expression can be written in terms of the error function, which is the foundation of the knife-edge technique. To model the knife-edge scan, we consider the blade moving vertically along the y-axis, partially blocking the beam from the bottom up. The transmitted power as a function of the blade position y' is then

$$P(y') = \int_{y'}^{\infty} \int_{-\infty}^{\infty} I(x,y)\,dx\,dy, \tag{3.3}$$

where the inner integral over x can be evaluated first:

$$\int_{-\infty}^{\infty} \exp\left(-\frac{2x^2}{w^2}\right) dx = \sqrt{\frac{\pi w^2}{2}}.$$

Up to this point the derivation has assumed a beam centered at $y = 0$. In a real knife-edge experiment, however, the beam center generally appears at an offset position r_0 defined by the mechanical alignment and by the reference frame of the translation stage. The Gaussian factor must therefore be written as $\exp\left[-2(y - r_0)^2/w^2\right]$. Incorporating this shift, the remaining integral becomes

$$P(y') = I_0 \sqrt{\frac{\pi w^2}{2}} \int_{y'}^{\infty} \exp\left(-\frac{2(y - r_0)^2}{w^2}\right) dy.$$

To evaluate the remaining integral, we introduce the substitution

$$u = \frac{\sqrt{2}(y - r_0)}{w},$$

which brings the expression into the standard form of the error function [2], [13], [17]. Accordingly, the normalized and shifted transmission can be written as

$$T(y) = \frac{P(y)}{P_0} = \frac{1}{2}\left[1 - \operatorname{erf}\left(\frac{\sqrt{2}(y - r_0)}{w}\right)\right], \tag{3.4}$$

where r_0 is the beam center along the y-axis, w is the $1/e^2$ beam radius at position z, and the error function erf arises from the Gaussian integration. Equation (3.4) describes the characteristic sigmoidal curve observed during a knife-edge scan. The transmission approaches unity ($T \to 1$) when the beam is unobstructed and decreases to zero ($T \to 0$) as the blade completely blocks the beam. A more detailed justification of the error-function dependence and its relation to Gaussian beam parameters is provided in the practical considerations section. Importantly, the beam radius w extracted from this method corresponds to the transverse width at the scanning plane z.

3.1 Beam Waist Estimation Methods

There are several ways of extracting the beam waist from the knife edge information. Some of them are discussed below.

3.1.1 10–90% Width Approximation

The 10–90% knife-edge approximation provides a simple and practical way to estimate the Gaussian beam radius using only two points of the transmission curve. Let y_{10} and y_{90} denote the positions where the normalized transmitted power satisfies $T(y_{10}) = 0.10$ and $T(y_{90}) = 0.90$. Using the analytical knife-edge model (3.4), we introduce the dimensionless variable

$$\xi = \frac{\sqrt{2}(y - y_0)}{w}.$$

With this substitution, the transmission becomes

$$T(\xi) = \tfrac{1}{2}\left[1 - \operatorname{erf}(\xi)\right].$$

The 10–90% knife-edge points therefore satisfy

$$0.10 = \tfrac{1}{2}[1 - \operatorname{erf}(\xi_{10})], \qquad 0.90 = \tfrac{1}{2}[1 - \operatorname{erf}(\xi_{90})],$$

from which

$$\operatorname{erf}(\xi_{10}) = 0.80, \qquad \operatorname{erf}(\xi_{90}) = -0.80.$$

Thus,

$$\xi_{10} = \operatorname{erf}^{-1}(0.8), \qquad \xi_{90} = -\operatorname{erf}^{-1}(0.8).$$

Returning to the spatial coordinate using

$$y = y_0 + \frac{w}{\sqrt{2}}\,\xi,$$

we obtain

$$y_{10} = y_0 + \frac{w}{\sqrt{2}}\operatorname{erf}^{-1}(0.8), \qquad y_{90} = y_0 - \frac{w}{\sqrt{2}}\operatorname{erf}^{-1}(0.8).$$

The corresponding 10–90% knife-edge width is therefore

$$\Delta y = y_{90} - y_{10} = \sqrt{2}\,w\,\operatorname{erf}^{-1}(0.8).$$

Solving for the beam radius gives

$$w = \frac{\Delta y}{\sqrt{2}\,\operatorname{erf}^{-1}(0.8)}.$$

Since $\operatorname{erf}^{-1}(0.8) \approx 0.90619$, the denominator becomes

$$\sqrt{2}\,\operatorname{erf}^{-1}(0.8) \approx 1.28155,$$

leading to the practical approximation

$$w \approx 0.78\,\Delta y.$$

In terms of the full beam diameter $D = 2w$, this yields

$$D \approx 1.56\,\Delta y.$$

This 10–90% approximation offers a fast and reasonably accurate estimate of the beam size using only two points of the knife-edge curve, avoiding the need for a full nonlinear fit [10], [18]. It was successfully employed as early as the 1970s for measuring micrometer-scale focused beams [10], and it remains a common informal beam diagnostic in many laboratory settings. The method relies on several simplifying assumptions about the beam and the data. First, it assumes an ideal Gaussian beam profile that is perfectly symmetric and centered relative to the knife-edge translation. Any deviation from a pure Gaussian, such as higher-order modes or an elliptically distorted beam, will

skew the knife-edge transmission curve and can introduce error in the inferred waist. The method also presumes that the power measurements at the 10% and 90% levels are accurate and not significantly affected by noise or drift. In practice, using only two data points makes the calculation highly sensitive to noise and baseline offsets: even small fluctuations in the power readings can lead to considerable uncertainty in the determined Δy and hence in w_0. Experimental applications should involve averaging repeated knife-edge scans and carefully accounting for background power levels when determining P_{10} and P_{90} [18]. Moreover, this two-point definition has been explicitly recognized in the ISO standardization framework as one of the permitted procedures for beam width determination [19].

3.1.2 Nonlinear Least-Squares Fit

A highly robust approach to knife-edge beam profiling consists in fitting the entire transmission curve to the theoretical complementary error function model [13], [18]. As previously discussed in Eq. (3.4), the transmitted power during a knife-edge scan is well described by the error function of a Gaussian beam profile. Instead of relying on a two-point approximation or on the derivative of noisy data, the nonlinear least-squares method uses all recorded data points to reconstruct the transmission curve and extract the beam parameters simultaneously. While Eq. (3.4) provides the normalized theoretical profile, experimental data is typically not normalized and directly measures transmitted power. In practice, the fitting model can be expressed as

$$P(y) = \frac{P_0}{2}\left[1 - \operatorname{erf}\left(\frac{\sqrt{2}(y - r_0)}{w}\right)\right], \tag{3.5}$$

where P_0 is the total power, r_0 the beam center position, and $w(z)$ the beam radius at the measurement plane z. Nonlinear regression (typically via the Levenberg–Marquardt algorithm) provides best-fit estimates of these coefficients for each transverse scan. The fitted beam radii $w(z)$ are then plotted as a function of the axial position z and fitted again to the Gaussian beam propagation law

$$w(z) = w_0\sqrt{1 + \left(\frac{z - z_0}{z_R}\right)^2}, \qquad z_R = \frac{\pi w_0^2}{\lambda}, \tag{3.6}$$

with w_0 is the minimum beam waist, z_0 its axial location, and z_R the Rayleigh range. This two-step fitting process yields a precise and consistent estimation of the beam waist and propagation parameters. The nonlinear fitting process makes use of all available data points, reducing the impact of noise at any single position and providing significantly lower uncertainty compared to derivative or threshold-based methods [13]. In addition, the regression provides statistical error bars and a covariance matrix, enabling rigorous uncertainty analysis and diagnostic checks such as residual evaluation. This approach has been shown to yield repeatability at the few-percent level in experimental implementations, even under moderate misalignments. It is also versatile: extensions of the fitting model allow the characterization of elliptic, astigmatic, or multimode beams

by introducing additional parameters [11]. The main drawbacks are its increased computational complexity and its dependence on good initial parameter guesses for convergence. In cases of poor signal quality or large mechanical artifacts, the fitting routine may converge to local minima or produce unstable results. Moreover, the method assumes a one-dimensional Gaussian profile; beams with pronounced non-Gaussian structure require modified models or generalized fitting functions [13]. Nevertheless, with appropriate experimental care, nonlinear least-squares fitting is considered the most reliable and accurate method among knife-edge analysis techniques. This method provides a rigorous framework for extracting the beam waist radius w_0, its axial position z_0, and the Rayleigh range z_R. Compared to simple approximations such as the 10-90% method, it is more robust, less sensitive to noise, and inherently provides confidence intervals, making it the method of choice for precision beam waist characterization [13], [19]

3.1.3 Derivative Method

One of the earliest analytical approaches to extract the beam radius from knife-edge measurements was proposed by Arnaud and co-workers in the 1970s [20]. The principle is straightforward: the transmitted power $P(y)$ measured during a knife-edge scan of a Gaussian beam follows a complementary error function, since it represents the cumulative integral of the Gaussian irradiance distribution. Explicitly, for a beam centered at r_0 with $1/e^2$ radius w, the transmitted power is

$$P(y) = \frac{P_0}{2}\left[1 - \operatorname{erf}\left(\frac{\sqrt{2}(y - r_0)}{w}\right)\right],$$

Differentiating Eq. (3.5) with respect to the knife-edge position y yields

$$\frac{dP(y)}{dy} = \sqrt{\frac{2}{\pi}}\frac{P_0}{w}\exp\left[-\frac{2(y - r_0)^2}{w^2}\right], \tag{3.7}$$

which is a Gaussian function with the same width parameter w as the original beam. Thus, the beam profile can, in principle, be recovered directly by numerically differentiating the measured transmission curve and fitting the result to a Gaussian. The beam radius w is then obtained from the width of the derivative profile, while r_0 corresponds to the beam center position. This approach has the advantage of theoretical elegance: it provides a direct inversion from cumulative data to the local intensity distribution, avoiding the need to work with integrated profiles [21]. In practice, however, the derivative method suffers from a critical drawback: numerical differentiation strongly amplifies experimental noise and small fluctuations in the measured power signal. As discussed in later analyses [13], [22], [23], this results in a broadened and noisy derivative curve, reducing the confidence in the fitted beam radius. Attempts to mitigate this effect using smoothing or filtering introduce an additional bias, typically overestimating the beam width due to artificial broadening of the Gaussian profile [13]. For this reason, although the derivative method was historically influential, its experimental implementation often proved less reliable than expected.

3.1.4 Linear Approximation at the Beam Center

A further simplification of the knife-edge analysis consists in linearizing the transmission curve around the beam center. Near the point where the knife-edge blocks half of the beam power, the error function in Eq. (3.5) can be approximated by its tangent, resulting in a locally linear relation between transmitted power and knife-edge displacement. This method was formalized in early studies of knife-edge profiling [17] and is occasionally used in applications requiring rapid position sensing. Mathematically, expanding the error function around $y = r_0$ gives

$$\frac{P(y)}{P_0} \approx \frac{1}{2} - \frac{1}{\sqrt{2\pi}\, w}\,(y - r_0), \tag{3.8}$$

so that the local slope at the beam center is

$$m = \left|\frac{dP}{dy}\right|_{y=r_0} = \frac{P_0}{\sqrt{2\pi}\, w}.$$

Rearranging this relation, the beam radius can be estimated as

$$w \approx \sqrt{\frac{2}{\pi}}\,\frac{P_0}{m}. \tag{3.9}$$

In this sense, the beam waist is inferred directly from the slope of the transmission curve at its inflection point, without fitting the entire dataset. The linear approximation method is extremely simple, requiring only the measurement of the slope at a single point rather than a full knife-edge scan. This makes it attractive for real-time beam monitoring or as a feedback signal in beam stabilization systems, where the absolute beam waist value is less critical than detecting small beam displacements or fluctuations [17]. Despite its simplicity, the method is not suitable for precise beam characterization. Because it relies on a local linearization, it assumes a perfectly Gaussian and symmetric beam and is highly sensitive to measurement noise in the derivative near y_0. Even small baseline drifts or power fluctuations can cause large errors in the slope estimate, and hence in w. Moreover, it provides no information about the beam propagation (waist position z_0, Rayleigh range z_R, or quality factor M^2). For these reasons, linear approximations are generally restricted to position-sensing or qualitative monitoring contexts and are not recommended for quantitative laser beam profiling [18]. Recent implementations, such as the chopper-based characterization proposed by Ortega *et al.*, have revisited this linear slope principle to obtain fast electrical signals proportional to the beam size, though with the same limitations in absolute accuracy [15].

3.1.5 Dithering Knife-Edge Method

An important refinement of the classical knife-edge technique is the so-called dithering knife-edge method, introduced to overcome noise limitations in high-sensitivity beam diagnostics [24]. The idea is to oscillate ("dither") the knife-edge at a small amplitude and fixed frequency while it is translated slowly across the beam. The transmitted optical power then contains a modulated component at the dithering frequency, which can be extracted using a lock-in amplifier. The resulting signal is proportional to the

derivative of the cumulative transmission curve, effectively reproducing the Gaussian irradiance profile without the need for numerical differentiation.

Mathematically, if the transmitted power as a function of knife-edge position y is $P(y)$, dithering the blade around x with a small amplitude δ yields a modulated component

$$P_{\mathrm{ac}}(y) \approx \delta \frac{dP(y)}{dy},$$

where P_{ac} is the amplitude of the lock-in detected signal. Since $\frac{dP}{dy}$ is Gaussian [see Eq. (3.7)], the lock-in output directly traces the beam's intensity distribution with a signal-to-noise ratio (SNR) enhanced by orders of magnitude compared to raw power measurements [24]. In practice, SNR values as high as 10^6:1 have been reported, which makes the dithering method comparable to scanning-slit profilometry in terms of resolution but with the simplicity of a knife-edge setup.

The dithering method combines the simplicity of the knife-edge arrangement with the robustness of lock-in detection. By modulating the edge and detecting only the ac component, the system strongly suppresses low-frequency noise, drift, and detector offsets. This enables precise reconstruction of the Gaussian profile and highly accurate beam width estimation, even in the presence of significant background fluctuations. Furthermore, the equivalence to a slit scan means that the technique can be extended to non-Gaussian or multimode beams, as the lock-in output still follows the local irradiance distribution [19]. On the other hand, the method requires additional instrumentation beyond the basic knife-edge setup: a mechanical actuator capable of stable dithering, and a lock-in amplifier to demodulate the signal. This increases cost and complexity, making it less practical for standard academic laboratories, where simpler knife-edge scans or camera-based profilers are preferred. Moreover, while the lock-in suppresses noise, it also limits the measurement bandwidth; the method is not suitable for studying fast temporal beam fluctuations or pulsed beams with low repetition rates. Another consideration is that the dithering amplitude must be carefully controlled: too large a modulation distorts the effective profile, while too small reduces the lock-in signal strength. It is particularly suited for metrology-grade applications where accuracy at the sub-micrometer level is required, but is seldom implemented in routine academic setups due to its reliance on specialized electronics [15], [24].

3.2 Practical Considerations for Knife-edge Measurements

While the knife-edge technique is a powerful and simple method for laser beam profiling, its successful implementation requires attention to several theoretical and experimental aspects to ensure accurate results. This section outlines key considerations and practical recommendations for applying the method effectively.

3.2.1 Parameter Definitions and Interpretation

A precise understanding of the beam parameters is essential for interpreting knife-edge measurements correctly. The beam radius w is conventionally defined as the distance at which the intensity falls to $1/e^2$ of its on-axis value. In the knife-edge technique, however, the detector does not measure the local intensity but the cumulative transmitted

power. Mathematically, this requires integrating the Gaussian intensity profile, and the resulting change of variables introduces a factor of $\sqrt{2}$ in the argument of the error function. This factor originates purely from the integral form of the transmission model and does not alter the physical meaning of w: the fitting parameter obtained from the knife-edge expression corresponds directly to the standard $1/e^2$ beam radius. Consequently, no additional scaling or correction is required. The details of the fitting procedure and its implementation are presented in the following section [2], [19], [25], [26]. It should be noted that other beam parameters can also be misinterpreted if their definitions are not explicitly stated. Common examples include confusing the beam radius w with the full beam diameter $2w$, interpreting the fitted amplitude without considering variations in total optical power or detector response, and attributing apparent shifts in the beam center to optical misalignment when they may instead result from knife-edge tilt or diffraction effects. Furthermore, an incorrect scaling of w propagates directly into derived quantities such as the waist w_0, the Rayleigh range z_R, and the beam-quality factor M^2, highlighting the importance of consistent parameter definitions throughout the analysis [2], [13], [26].

3.2.2 Diffraction Effects and Sensor Size

To minimize diffraction effects at the blade edge, the condition $\lambda \ll w$ must be satisfied. When this holds, edge diffraction does not significantly alter the power measurement. Otherwise, systematic errors may be introduced, particularly when the waist approaches only a few times the wavelength, as pointed out by Nemoto [23]. Additionally, the detector size is a critical factor. In this work, it is assumed that the detector area is larger than the beam cross-section at the measurement plane, allowing the total transmitted power to be accurately captured. Wright emphasized that insufficient detector area can bias the integrated signal, leading to artificially reduced beam widths [19]. If the detector is too small, two options can mitigate spatial averaging errors: (1) coupling the detector to an integrating sphere, or (2) using a lens with a large numerical aperture to collect and focus the light onto the active area of the sensor [13], [18].

3.2.3 Experimental Best Practices

Accurate knife-edge measurements rely not only on the theoretical formulation of the method but also on several experimental conditions that determine its precision and reproducibility. These considerations bridge the gap between the analytical assumptions discussed in this chapter and their implementation in a real optical setup. The following guidelines summarize the main factors identified in the literature as critical for reliable beam characterization [13], [19], [22]:

- The knife-edge should be long and sharp enough to fully intercept the beam across its transverse dimension, minimizing diffraction and partial clipping effects.
- The translational motion must be smooth and use sufficiently small step sizes to resolve the transition in transmitted power accurately.
- Measurements should be repeated at several axial positions z to reconstruct the propagation curve $w(z)$ and confirm the Gaussian nature of the beam.

- The detector must operate in its linear regime; if its active area is small, an integrating sphere or lens can be used to collect the transmitted power efficiently.
- Ambient light and mechanical vibrations should be minimized to maintain a stable baseline and improve the signal-to-noise ratio.

Adhering to these practices ensures that the measured parameters, such as the beam radius $w(z)$ and center position r_0, are representative of the actual optical field rather than artifacts of the measurement process. The practical implementation of these considerations, along with specific details of the acquisition system and control software, is discussed in the next chapter.

Chapter 4

Automated Acquisition and Control System

Reliable characterization of laser beams using the knife-edge technique requires accurate synchronization between the displacement of the blade and the acquisition of optical power. Manual operation of the setup introduces uncertainties associated with positioning, alignment, and timing, which compromise the accuracy of the extracted beam parameters. To overcome these limitations, an automated acquisition and control system was developed. The system integrates both hardware and software elements to achieve fully automated measurements. On the hardware side, an optical power meter Thorlabs PM100D, focal lens, a knife and a motorized translation stage were employed. On the software side, a MATLAB-based application was designed to interface with the instruments, automate the movement of the blade, acquire and store data, and perform real-time curve fitting. This integration not only reduces human error but also enables the repetition of measurements under controlled and reproducible conditions.

4.1 System Overview

A continuous-wave He–Ne laser operating at 543.5 nm and 1.5 mW serves as the light source. The knife-edge is mounted on a motorized translation stage aligned with the propagation axis of the beam. The transmitted power after the knife-edge is detected by the Thorlabs PM100D power meter, and the resulting signal is acquired and processed by a custom MATLAB application. The motorized stage is driven by stepper motors controlled through an Arduino board running the GRBL firmware, which interprets G-code commands for precise linear motion. The automated system integrates the optical arrangement with the detection unit and the control software, forming a compact framework for knife-edge measurements. The overall architecture of the automated system is illustrated in Fig. 4.1b, where the interaction between the optical components, detection hardware, and control software is summarized. The MATLAB application acts as the central hub, coordinating the communication with both the power meter and the translation stage, while simultaneously storing the acquired data in structured files for further processing.

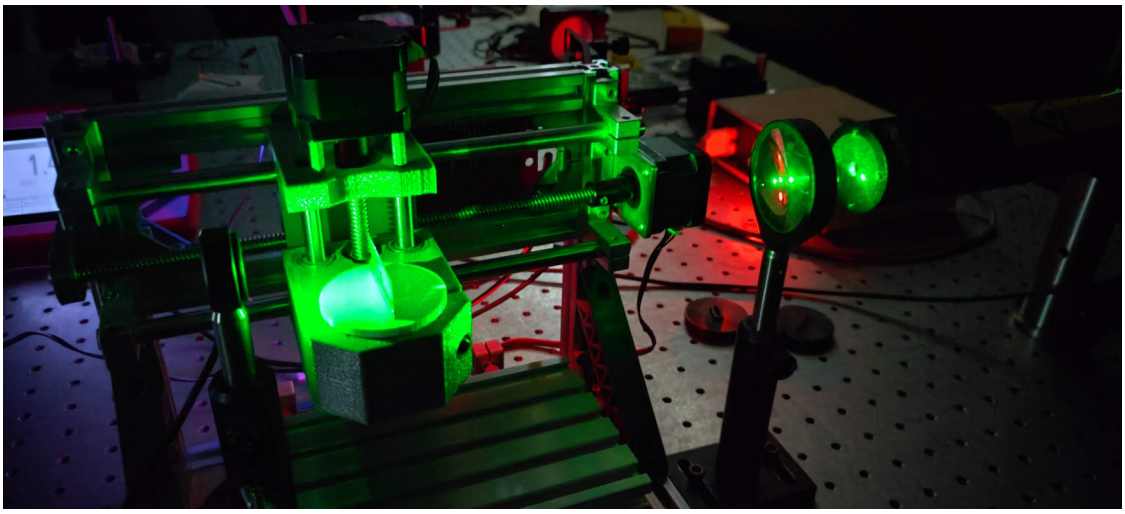

(A) Automated acquisition and control setup integrating the laser source, knife-edge mounted on the translation stage, and optical power meter.

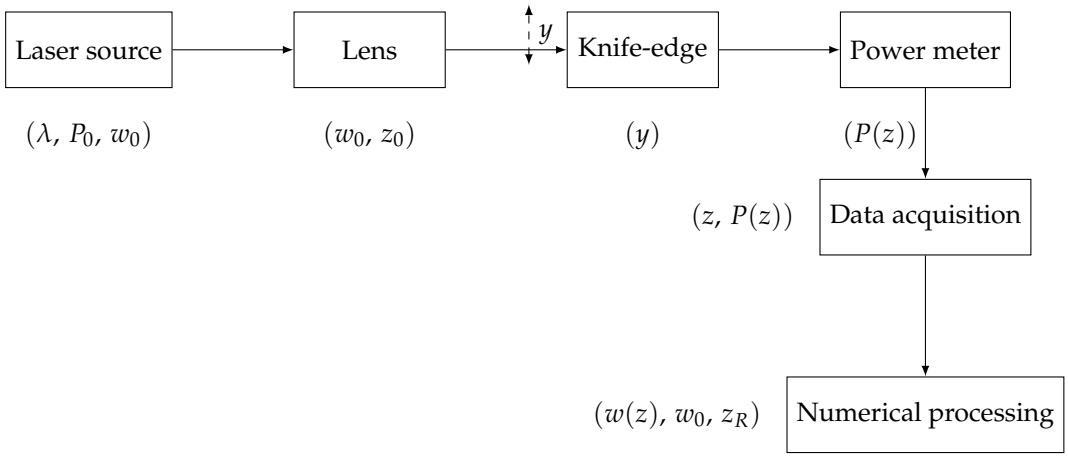

(B) Block diagram of the automated acquisition and control system. Below each block are the principal variables related to each process.

FIGURE 4.1: Automated knife-edge measurement system. (a) Experimental setup. (b) Schematic block diagram of the experimental array.

4.2 Hardware Implementation

The reliable characterization of Gaussian beams and their propagation parameters requires precise control of both the optical and mechanical components involved in data acquisition. To achieve the accuracy demanded by the knife-edge technique, the experimental system must ensure stable beam alignment, reproducible blade displacements, and synchronized power readings with high temporal resolution. In this work, a compact and fully automated arrangement was developed to meet these requirements, integrating commercial and custom-built hardware through a MATLAB-based interface. The hardware implementation is composed of two main subsystems: an optical power meter, responsible for detecting and recording the transmitted power during the knife-edge scans, and a motorized translation stage, which provides controlled and repeatable motion of the blade along the transverse axis. The communication between both devices and the computer enables coordinated operation, minimizing human error and enhancing measurement consistency across repeated scans. The following subsections describe the specifications and configuration of each component in detail.

4.2.1 Optical Power Meter

The optical power measurements were carried out with a Thorlabs PM100D console, a versatile instrument designed to operate with a wide range of photodiode, thermal, and pyroelectric sensors. According to the manufacturer, the PM100D provides a dynamic range exceeding 100 dB when used with photodiodes and a measurement bandwidth up to 100 kHz, ensuring accurate detection of small power variations during beam profiling [27]. The unit communicates with a computer via USB and supports SCPI-compatible drivers as well as MATLAB libraries, which facilitated the development of automated acquisition routines. Additional functions such as wavelength correction and relative power monitoring contribute to improving the reliability of the measurements. The console was coupled to an S120C photodiode sensor, specified for operation in the 400-1100 nm spectral range with a maximum measurable power of 50 mW. This range adequately covers the emission wavelength of the He-Ne laser employed in the experiments. The detector head has an active area of approximately 9.5 mm in diameter, which ensured full collection of the transmitted beam behind the knife-edge without significant clipping. In the knife-edge setup, the PM100D–S120C system reliably recorded the transmitted power as the blade scanned across the beam, providing the normalized transmission curves required for Gaussian beam analysis.

4.2.2 Motorized Translation Stage

The displacement of the knife-edge was automated using a custom translation stage driven by stepper motors. The motors are controlled through an Arduino board running the GRBL firmware, which interprets G-code commands to produce precise linear motion. This configuration allows movements with step sizes down to tenths of a millimeter, ensuring sufficient resolution for the knife-edge technique. The Arduino communicates with the MATLAB application through a virtual COM port. This makes it possible to send displacement commands and synchronize the motion of the stage with the power measurements from the PM100D. The modularity of the design also enables future extensions, such as multi-axis motion or integration with additional detectors.

4.3 Software Development

The control and acquisition tasks were implemented in a MATLAB App specifically designed for this project. The application provides a graphical user interface organized into three main tabs: *Adquisición*, *Estimación*, and *Ajustes*. Each tab contains the functionalities required to perform knife-edge measurements and beam waist estimation in an automated manner. The following subsections describe each interface.

4.3.1 Acquisition Tab

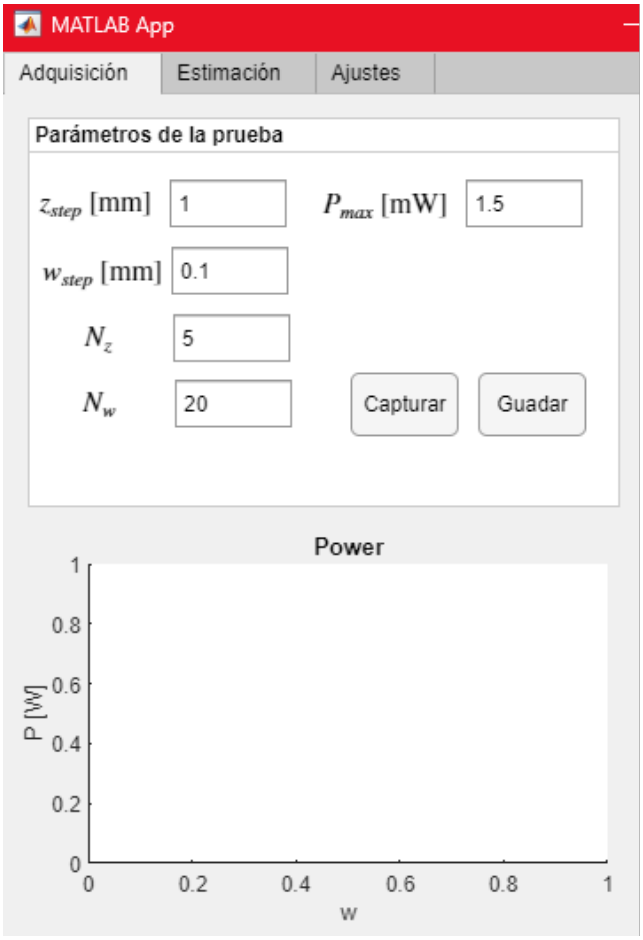

FIGURE 4.2: Acquisition tab of the MATLAB App.

The *Acquisition* tab defines the parameters of the experimental run. The user specifies the axial step size Δz, the transverse step size Δw, the number of measurement positions along the propagation axis N_z and across the beam profile N_w, as well as the maximum expected optical power $P_{\max}$. Once configured, the interface provides buttons to capture new datasets and to store them in structured `.mat` files for further processing. The lower panel of the tab displays a real-time plot where each knife-edge cut is added upon completion, allowing the user to monitor the measurement process and

verify data consistency as the scan progresses. In this way, the *Acquisition* tab establishes the baseline configuration for reproducible beam profiling experiments, enabling automated sequences with minimal manual intervention.

4.3.2 Estimation Tab

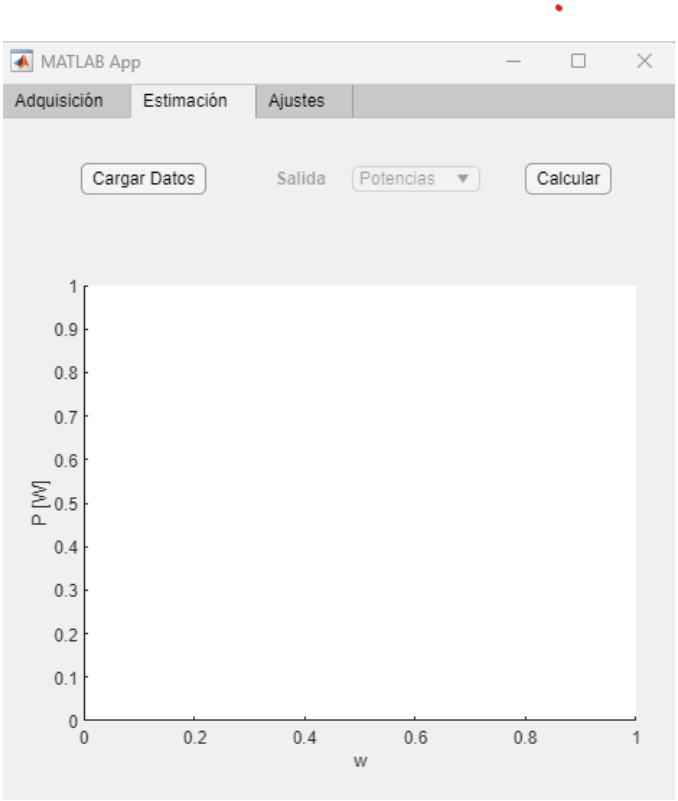

FIGURE 4.3: Estimation tab of the MATLAB App.

The *Estimation* tab is dedicated to the processing and analysis of the acquired data. Transmission curves obtained from knife-edge scans can be loaded from previously stored files, visualized, and selectively plotted. The user can choose which cut to display, facilitating the inspection of individual measurements and the identification of possible anomalies. The core functionality of this tab is the nonlinear curve fitting of the transmission data to the theoretical error function model. From this fitting procedure, the main beam parameters are extracted: the maximum transmitted power $P_{\max}$, the beam center r_0, and the beam radius $w(z)$ at each measurement plane. In addition, the tab provides an estimation of the fundamental waist parameter w_0, which represents the minimum spot size of the Gaussian beam. Beyond the analysis of individual cuts, the software implements a global fitting routine for the evolution of the beam radius along the propagation direction. By fitting $w(z)$ to the Gaussian beam propagation law 2.4

$$w(z) = w_0 \sqrt{1 + \left(\frac{z - z_0}{z_R} \right)^2},$$

the program yields the beam waist radius w_0, its axial location z_0, and the Rayleigh range z_R. This feature allows the user to obtain a consistent and physically meaningful characterization of the beam, consolidating multiple measurements into a unified description of the propagation parameters.

4.3.3 Settings Tab

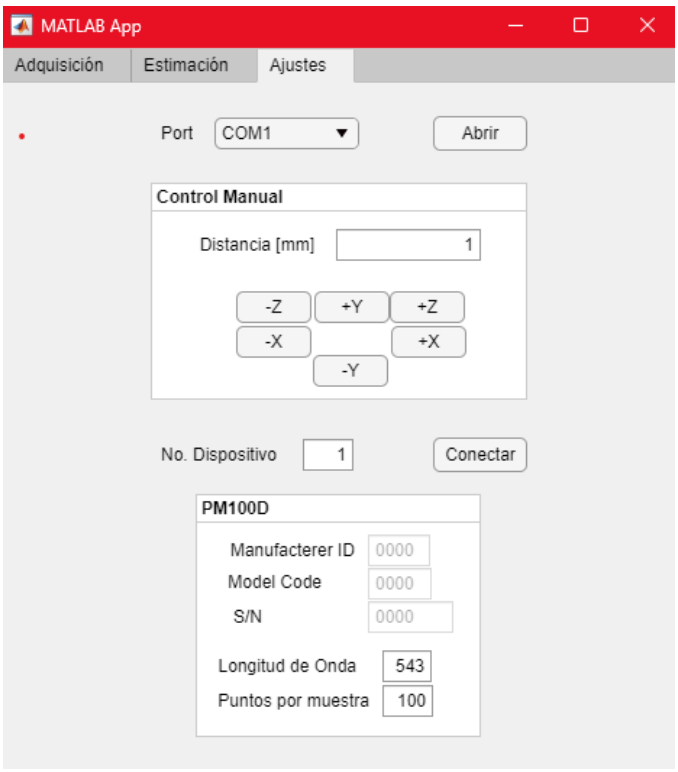

FIGURE 4.4: Settings tab of the MATLAB App.

The *Settings* tab allows the user to establish communication with the connected devices. The translation stage is connected via a serial COM port, so the interface includes functions to scan available ports and select the appropriate one. In addition, manual control buttons are provided to displace the stage along the X, Y, and Z axes by a user-defined step size, enabling both coarse positioning and fine alignment of the beam. The lower panel of the tab corresponds to the Thorlabs PM100D optical power meter. When the *Connect* button is pressed, the application initializes communication with the instrument through a VISA interface. Internally, the connection routine relies on VISA drivers provided by Thorlabs. The software searches for instruments by serial number, and if the connection is successful, the manufacturer ID, model code, and serial number of the device are automatically retrieved and displayed in the interface. These fields are set to read-only mode to prevent accidental modification. Additional controls allow the user to configure the measurement parameters of the PM100D, including the operating wavelength and the number of samples per acquisition.

4.3.4 Remarks on Code Integration

The MATLAB App was developed by adapting an existing framework for device communication and graphical interface management. The main contribution of this work lies in the implementation of an improved fitting algorithm for beam radius estimation, as well as in the integration of global waist propagation analysis. While the underlying code structure was inherited, the modifications introduced significantly enhance the accuracy and robustness of the knife-edge measurements.

4.4 Integration and Workflow

The operation of the automated system follows a straightforward sequence:

1. Initialization of the MATLAB application and connection with devices.
2. Selection of measurement parameters, such as displacement range and step size.
3. Automated displacement of the knife-edge using the motorized stage.
4. Simultaneous acquisition of transmitted power values from the PM100D.
5. Storage of results in structured files for further analysis.
6. Execution of curve fitting routines to estimate beam parameters in real time.

This workflow ensures that each measurement is carried out under consistent conditions, improving both reproducibility and accuracy compared to manual operation.

4.5 Data Acquisition

The data acquisition process was implemented through a custom MATLAB App designed to coordinate the motion of the translation platform and the readings of the optical power meter. The system establishes serial communication with the GRBL controller that drives the stepper motors and with the Thorlabs PM100D console, allowing fully automated knife-edge scans under predefined spatial and temporal parameters.

Once communication is verified, the application initializes the acquisition matrices `potdata`(z, w) and `coef`(z), together with the position vectors `zdata` and w`data`, defined by the step sizes `zstep` and w`step`. The scanning sequence is structured in a nested loop: the external iteration corresponds to the longitudinal coordinate z_i, while the internal loop performs a transverse displacement of the knife-edge along w, collecting the transmitted power $P(z_i, w_j)$ at each step. Each power value acquired by the PM100D results from the internal averaging of approximately 100 rapid samples performed by the instrument's firmware. To further enhance stability, the MATLAB application performs an additional external averaging routine: for each knife-edge position, `numMediciones = 10` consecutive readings are requested from the console, each separated by a 100 ms delay, and their mean value is stored as $P(z_i, w_j)$. This two-stage averaging process minimizes both high-frequency electronic noise and slower temporal fluctuations in the laser output, ensuring consistent power readings across the entire scan. After each sweep in w, the stage returns to its initial position by reversing the accumulated displacement

command through the GRBL interface, ensuring repeatable alignment for the next axial position. The scanning commands are sent in incremental mode (`G01`) with controlled feed rates of 450 mm/min (transverse) and 300 mm/min (axial), corresponding to stable mechanical operation of the motion system.

During the acquisition, each completed profile is plotted in real time on the App interface, providing immediate feedback on the signal quality and potential anomalies such as misalignment or power drift. Once all N_z scans are completed, the platform automatically returns to the reference position ($z = 0$), and the resulting matrix $\mathbf{P}(z, w)$ is stored in memory with the flag `new_data_available` set to one, signaling that the dataset is ready for post-processing. The acquired data therefore consist of averaged power traces $P(z_i, w_j)$ for discrete axial positions, each representing the cumulative intensity transmitted through the knife-edge aperture. These traces are subsequently used to reconstruct the beam propagation and extract the relevant Gaussian parameters.

Chapter 5

Data Fitting and Numerical Processing

The experimental implementation of the knife-edge technique provides a set of power transmission curves that must be analyzed in order to extract the relevant beam parameters. Raw measurements, however, are not sufficient by themselves, as noise, alignment imperfections, and instrumental limitations can affect the accuracy of the results. For this reason, numerical processing and data fitting are required to obtain reliable parameters that characterize the Gaussian beam profile. In this chapter, the mathematical models employed to describe the transmitted power and the beam waist evolution are presented. The fitting procedures implemented in MATLAB are discussed, along with the numerical strategies used to ensure convergence and robustness. These methods allow for the estimation of beam waist, beam center, and maximum transmitted power from the experimental data. Additionally, global fitting of the waist evolution along the propagation axis is carried out, providing an accurate determination of the minimum waist value and its position. The results of this numerical analysis establish the basis for subsequent comparison with theoretical models, and they serve as a crucial step in validating the experimental approach to laser beam characterization.

5.1 Curve Fitting Approach

Experimental measurements rarely follow an ideal analytical expression due to random noise, alignment imperfections, and instrumental limitations. For this reason, a curve-fitting procedure is required to extract the underlying parameters of the Gaussian beam from the knife-edge data. Curve fitting consists of selecting a mathematical model, defining its parameters, and adjusting those parameters so that the model best represents the experimental data according to a statistical criterion, typically the least-squares minimization [28], [29]. In general, the nonlinear least-squares problem can be formulated as the minimization of the objective function

$$S(b) = \sum_{i=1}^{N} \left[y_i - f(x_i, b) \right]^2, \tag{5.1}$$

where y_i are the measured data points, $f(x_i, b)$ is the model function depending on the independent variable x_i and on the parameter vector $b = [b(1), b(2), \ldots, b(M)]^\top$, with $(\cdot)^\top$ denoting the transpose. The function $S(b)$ represents the sum of squared residuals. The solution $\hat{b}$ that minimizes $S(b)$ corresponds to the parameter vector that

provides the best fit to the data under the least-squares criterion. For nonlinear models, this optimization cannot be solved analytically; instead, an iterative algorithm is used to approximate the minimum by successive linearizations of the model function [30], [31].

5.1.1 MATLAB Implementation

In this work, all curve fittings were performed using the `fitnlm()` function provided in MATLAB's Statistics and Machine Learning Toolbox [32]. This routine implements a nonlinear least-squares regression based on the Levenberg–Marquardt algorithm, a hybrid optimization scheme that combines the efficiency of the Gauss–Newton method with the numerical stability of gradient descent [30], [31]. At each iteration, the model $f(x, b)$ is linearized around the current estimate b_k using a first-order Taylor expansion:

$$f(x, b) \approx f(x, b_k) + J(b_k)\,(b - b_k),$$

where $J(b_k)$ is the Jacobian matrix of partial derivatives $\partial f / \partial b_j$ evaluated at b_k and $(\cdot)^\top$ denotes matrix transpose. The parameter vector is then updated according to

$$b_{k+1} = b_k + \delta b,$$

with

$$(J^\top J + \lambda I)\,\delta b = J^\top \left[y - f(x, b_k)\right],$$

where λ is a damping factor that balances between the Gauss–Newton and gradient-descent behaviors. When λ is small, the algorithm behaves like Gauss–Newton, converging rapidly near the minimum; when λ is large, it becomes more stable but slower, following the gradient direction. The iterations continue until the relative change in $S(b)$ or in the parameters falls below a predefined tolerance. To increase robustness against outliers and spurious points in the power measurements, a robust weighting scheme was applied through the `RobustWgtFun` option of `fitnlm`, using the `bisquare` function. This weighting modifies the effective contribution of each residual to the objective function:

$$S(b) = \sum_{i=1}^{N} w_i \left[y_i - f(x_i, b)\right]^2, \tag{5.2}$$

where w_i are adaptive weights that decrease for large residuals, effectively down-weighting the influence of outliers. Such robust regression approaches are especially valuable when dealing with optical measurements, where fluctuations in laser power or detector response can produce occasional anomalies [29], [33].

5.1.2 Parameterization and Outputs

The function `fitnlm()` requires that the fitting model be expressed as a function of a parameter vector `b`. For this reason, all physical quantities in the Gaussian-beam model were mapped onto the coefficient vector b, such that

$$b(1) \to r_0, \quad b(2) \to w, \quad b(3) \to P_0$$

for the knife-edge transmitted power model, and

$$b(1) \to w_0, \quad b(2) \to z_0, \quad b(3) \to z_R$$

for the beam waist evolution model. This parameterization allows the model equations to be defined as anonymous functions in MATLAB, which can then be supplied to `fitnlm()` together with the experimental data and the initial parameter estimates β_0. The provision of suitable initial guesses β_0 is essential for the convergence of nonlinear regression, as the iterative search for the minimum of Eq. (5.1) can otherwise be trapped in local minima or diverge if started far from the true solution [30], [31]. To ensure physical consistency and numerical stability, β_0 was initialized with values derived directly from the experimental dataset typically the beam center estimated from the scan midpoint, the beam width from the standard deviation of knife positions, and the maximum transmitted power from the peak value of the measured curve. For the propagation model, the initial guesses corresponded to the minimum measured beam width, the corresponding z position, and the theoretical Rayleigh range $\pi w_0^2/\lambda$. These informed initializations allowed the fitting routine to converge reliably across all datasets, minimizing the need for manual tuning.

The output of `fitnlm()` includes:

- the estimated coefficients $\hat{b}$,
- their standard errors and confidence intervals,
- the fitted (predicted) values $f(x_i, \hat{b})$,
- and statistical indicators such as the root mean square error (RMSE) and coefficient of determination R^2.

These quantities were subsequently used for evaluating the quality of each fit and for calculating secondary parameters such as alignment metrics and beam-propagation constants.

5.2 Mathematical Models for Curve Fitting

Two mathematical models were employed to extract the characteristic parameters of the laser beam from the knife-edge measurements. The first model describes the transmitted power as a function of the knife-edge position, while the second model accounts for the axial evolution of the beam waist. Both models were fitted to the experimental data using nonlinear least-squares regression with robust weighting (bisquare function), implemented via MATLAB's `fitnlm()` routine. This two-step approach allows first the local reconstruction of transverse beam profiles at different axial positions, and subsequently, the global characterization of the beam propagation parameters.Throughout this section we use the parameter vector $b = (b(1), b(2), b(3))^\top$ exactly as implemented in the code.

5.2.1 Knife-edge Transmitted Power Model

In this stage, a fitting loop was executed over all axial positions z_i to reconstruct the transverse transmission profile of the laser beam at each plane. For every z_i, the measured transmitted power $P(y)$ was modeled as a cumulative Gaussian distribution of the form:

$$P(y) = \frac{b(3)}{2}\left[1 - \mathrm{erf}\left(\frac{\sqrt{2}(y - b(1))}{b(2)}\right)\right], \tag{5.3}$$

where y represents the knife-edge position, and the parameters $b(1)$, $b(2)$, and $b(3)$ correspond to the beam-center position $b(1) \equiv r_0$, the beam radius at the detection plane $b(2) \equiv w$, and the maximum transmitted power $b(3) \equiv P_0$. Each transverse scan, corresponding to a fixed axial position z_i, was fitted to Eq. (5.3) to obtain the parameters $r_0(z_i)$, $w(z_i)$, and $P_0(z_i)$. To ensure convergence of the nonlinear regression, the algorithm was initialized with the following physically guided parameter vector:

$$\beta_0 = \begin{Bmatrix} \sigma_y, \\ y \text{ at } \max[P(y)], \\ P_{\max} \end{Bmatrix},$$

where σ_y is the standard deviation of the knife positions within the scan range, y denotes the knife-edge position at the maximum transmitted power, and $P_{\max}$ is the highest measured power value. This initialization approximates the beam radius from the dispersion of the data, sets the beam center near the upper boundary of the scan, and uses the largest measured power as the normalization constant. Such choices accelerate convergence and prevent the optimizer from falling into nonphysical local minima. To minimize the influence of random noise or spurious readings near the knife-edge cutoff, a robust weighting function (bisquare method) was applied during the regression. This option reduces the contribution of points with large residuals, improving the reliability of the fit in the presence of measurement artifacts. In practical terms, the bisquare weighting preserves the central region of the error function, where the derivative is largest, while down-weighting outliers in the low and high-power tails. The fitting was repeated for each z_i, resulting in N_z independent parameter sets. After each fit, the estimated coefficients $r_0(z_i)$, $w(z_i)$, and $P_0(z_i)$ were stored along with their standard errors, residuals, and R^2 values. These outputs form three primary vectors that describe the beam center trajectory, the local beam radius, and the total transmitted power as functions of z. This set of fitted parameters constitutes the input dataset for the second fitting stage, in which the beam propagation law is evaluated.

5.2.2 Beam Radius Evolution Model

Once the beam radius $w(z)$ had been determined for all axial positions z_i, a second nonlinear regression was performed to describe its evolution along the propagation direction. Under the paraxial approximation, the beam radius obeys the Gaussian propagation law:

$$w(z) = b(1)\sqrt{1 + \left(\frac{z - b(2)}{b(3)}\right)^2}, \tag{5.4}$$

where $b(1) \equiv w_0$ is the minimum beam waist, $b(2) \equiv z_0$ the axial waist position, and $b(3) \equiv z_R$ the Rayleigh range.

The fitting algorithm was initialized with the following physically guided estimates:

$$\beta_0 = \begin{Bmatrix} \min\{w(z)\}, \\ z \text{ at } \min\{w(z)\}, \\ \pi \, \min\{w(z)\}^2/\lambda \end{Bmatrix}.$$

These guesses respectively correspond to the smallest measured beam width, its position along the optical axis, and the theoretical Rayleigh range calculated from the laser wavelength. The same robust least-squares approach with bisquare weighting was adopted to ensure numerical stability against deviations from the ideal Gaussian model. The optimized parameters w_0, z_0, and z_R describe the global beam geometry, including its minimum waist, waist position, and divergence. The theoretical Rayleigh range $z_R^{(\text{theo})} = \pi w_0^2/\lambda$ was also computed and compared with the fitted value as an internal validation of the Gaussian-beam hypothesis. The resulting analytical curve $w(z)$ provides a concise quantitative description of the beam propagation, serving as the reference model for all subsequent optical characterizations.

5.2.3 Alignment and Stability Metrics via Quadratic Fitting

After obtaining the beam-center estimates $r_0(z_i)$ from the knife-edge fits at each axial position, an additional analysis was performed to quantify the stability and residual misalignment of the beam along propagation. Ideally, the beam center should remain constant as the translation stage moves, with any variation in $r_0(z)$ arising only from mechanical or optical misalignment. To evaluate these effects quantitatively, the measured beam centers were fitted to a quadratic model of the form

$$r_0(z) = az^2 + bz + c, \tag{5.5}$$

where a represents curvature (typically associated with small bowing of the translation axis or lens decentering), b corresponds to a net tilt of the system, and c is the offset at the reference plane. The adequacy of this model is assessed by the coefficient of determination

$$R^2_{\text{quad}} = 1 - \frac{\sum_i [r_0(z_i) - \widehat{r}_0(z_i)]^2}{\sum_i [r_0(z_i) - \bar{r}_0]^2}, \tag{5.6}$$

where $\widehat{r}_0(z_i)$ denotes the fitted quadratic trend and $\bar{r}_0$ the mean beam-center value. A high R^2_{quad} (typically above 0.9) confirms that the observed drift can be adequately described by a slow geometric curvature and a small linear tilt. From this fit, global stability indicators are extracted. The standard deviation of the beam center, σ_{r_0}, quantifies the absolute spatial stability, while its normalized form σ_{r_0}/w_0 provides a relative measure referenced to the beam size. At this stage of the analysis, the exact value of the

waist w_0 is not yet known, since it will be obtained in the subsequent global fit of $w(z)$; therefore, an approximate mean beam radius $\overline{w}$, computed from all local widths $w(z_i)$, is used in its place to estimate this ratio. This approximation introduces a negligible bias because the beam width varies slowly within the scanned region compared to the scale of misalignment being evaluated. The fitted curvature term az^2 is then subtracted from the experimental $r_0(z)$ values to remove slow mechanical bowing and isolate the residual tilt of the beam. A linear regression is subsequently performed on the corrected data,

$$r_0^{(\mathrm{corr})}(z) = r_0(z) - az^2 \simeq b_{\mathrm{corr}}\, z + c_{\mathrm{corr}}, \tag{5.7}$$

yielding the net slope b_{corr}, which expresses the beam's lateral drift per unit axial displacement. When r_0 is expressed in μm and z in mm, the slope has units of $\mu\mathrm{m/mm}$, which directly correspond to milliradians through the small-angle approximation

$$\theta \approx \arctan(b_{\mathrm{corr}}) \approx b_{\mathrm{corr}}\ (\mathrm{mrad}). \tag{5.8}$$

This provides a convenient estimate of the effective angular deviation of the beam relative to the propagation axis. To classify the alignment quality, two dimensionless quantities are considered: the normalized beam-center fluctuation σ_{r_0}/w_0 and the slope magnitude $|b_{\mathrm{corr}}|$, complemented by the goodness of the quadratic fit R^2_{quad}. A dataset is regarded as *well aligned* when $\sigma_{r_0}/w_0 < 0.01$, $|b_{\mathrm{corr}}| < 0.02\mu\mathrm{m/mm}$, and $R^2_{\mathrm{quad}} > 0.95$. If the relative deviation remains below 5% but the tilt or curvature slightly exceed these limits, the condition is considered *acceptable*. Larger values indicate significant misalignment, which may distort the beam-profile reconstruction and must be treated with caution. These metrics collectively provide a quantitative and geometry-aware assessment of the mechanical and optical stability of the system. They also serve as an internal validation step prior to the global waist fitting, ensuring that the $w(z)$ data are not biased by systematic off-centering. Datasets failing the "well aligned" condition are flagged for review, while those within the "acceptable" range can still be used for analysis but are interpreted with corresponding uncertainty margins.

Chapter 6

Applications of Beam Waist Determination in Nonlinear Optics

Quantitative nonlinear optics depends critically on the accurate determination of the optical intensity at the sample. In Gaussian beams, the on-axis intensity is governed by a single geometrical parameter, the beam waist w_0, through the relation $I_0 = 2P_0/(\pi w_0^2)$. Any fractional error in w_0 propagates quadratically to I_0 and directly to derived quantities such as the nonlinear refractive index n_2, the third-order susceptibility $\chi^{(3)}$, multiphoton absorption coefficients, or harmonic conversion efficiencies. In practice, the limiting factor in many nonlinear optical measurements is not the physical model itself, but the metrology of the beam—specifically, the ability to determine its size, shape, and axial evolution with traceable precision and reproducibility [1], [34], [35].

The phenomenological basis of nonlinear optics is well established: as the optical intensity increases, the induced polarization of a medium ceases to scale linearly with the applied field and must be expressed as a power-series expansion, $\mathbf{P}(t) = \epsilon_0[\chi^{(1)}\mathbf{E} + \chi^{(2)}\mathbf{E}^2 + \chi^{(3)}\mathbf{E}^3 + \cdots]$, from which emerge the fundamental nonlinear processes—harmonic generation, wave mixing, and, in centrosymmetric media, the third-order Kerr response described by $n(I) = n_0 + n_2 I$ [1], [34]. In all these cases, the explicit dependence on I_0 implies that accurate beam characterization, particularly of w_0, is indispensable for obtaining reproducible and comparable values of n_2 and $\chi^{(3)}$ [36], [37].

From a metrological perspective, determining w_0 is not a trivial geometric measurement. It requires defining an appropriate propagation model (typically Gaussian–paraxial), selecting a consistent beam-width criterion ($1/e$, $1/e^2$, or FWHM), and establishing a complete uncertainty budget that includes detector noise, power drift, astigmatism, beam quality factor M^2, alignment, and thermal effects in the setup [26], [38]. Among the available techniques, the knife-edge method offers robust traceability and minimal sensitivity to pixel quantization, saturation, or aberrations commonly encountered in camera-based profiling. Its reliability, however, depends on practical details such as aperture size, detector linearity, step resolution, mechanical hysteresis, and the precise alignment of the blade with the optical axis. These considerations are particularly critical in benchmark nonlinear optical techniques such as Z-scan, where the nonlinear phase shift $\Delta\phi_0 = k\, n_2\, I_0\, L_{\text{eff}}$ depends linearly on the peak intensity and thus quadratically on the beam waist [36], [37]. Consequently, even small errors in w_0 can lead to significant deviations in the extracted nonlinear parameters.

In this chapter, the precise determination of w_0 is directly connected to representative nonlinear optical applications, including Z-scan measurements, multiphoton absorption, harmonic generation, and Kerr-induced self-focusing. We show that an automated knife-edge system, integrating synchronized acquisition, averaging routines, and axial control, can significantly reduce experimental variance, detect systematic misalignments, and yield waist and Rayleigh range estimates with uncertainties compliant with international standards [1], [26].

6.1 Introduction to Nonlinear Optics

In classical linear optics, the response of a dielectric medium to an incident electromagnetic field is proportional to the field strength. The induced polarization $\mathbf{P}(t)$, which represents the dipole moment per unit volume, satisfies the simple relation

$$\mathbf{P}(t) = \epsilon_0 \chi^{(1)} \mathbf{E}(t), \tag{6.1}$$

where $\chi^{(1)}$ is the linear susceptibility and ϵ_0 is the vacuum permittivity. This linear approximation holds when the field is weak enough that the electronic restoring forces of the medium remain proportional to the applied field, implying that the superposition principle is valid and no new optical frequencies are generated. However, as the optical field intensity increases, typically when illuminated by coherent laser radiation, the induced polarization ceases to scale linearly with the field amplitude. The electrons bound to atoms or molecules experience anharmonic restoring forces, and the resulting polarization must be expressed as a power-series expansion in the electric field strength [34], [35]:

$$\mathbf{P}(t) = \epsilon_0 \left[\chi^{(1)} \mathbf{E}(t) + \chi^{(2)} \mathbf{E}^2(t) + \chi^{(3)} \mathbf{E}^3(t) + \cdots \right] = \sum_{n=1}^{\infty} \mathbf{P}^{(n)}(t). \tag{6.2}$$

Each term $\mathbf{P}^{(n)}(t) = \epsilon_0 \chi^{(n)} \mathbf{E}^n(t)$ represents the nonlinear polarization of order n, and the coefficients $\chi^{(n)}$ are the nth-order susceptibilities, which characterize the strength of the nonlinear response. For example, $\chi^{(2)}$ describes second-order phenomena such as second-harmonic generation (SHG) and sum-frequency generation, while $\chi^{(3)}$ governs third-order processes such as four-wave mixing, self-focusing, and the optical Kerr effect. In the framework of Maxwell's equations, the nonlinear polarization acts as a source term that generates new electromagnetic fields. The inhomogeneous wave equation in a nonlinear medium can be written as

$$\nabla^2 \mathbf{E} - \frac{n^2}{c^2} \frac{\partial^2 \mathbf{E}}{\partial t^2} = \frac{1}{\epsilon_0 c^2} \frac{\partial^2 \mathbf{P}_{\mathrm{NL}}}{\partial t^2}, \tag{6.3}$$

where $\mathbf{P}_{\mathrm{NL}}$ represents the nonlinear part of the polarization. This equation shows that a time-varying nonlinear polarization can radiate new optical frequencies, allowing energy exchange between interacting waves. As discussed by Powers [35], the inclusion of nonlinear terms in $\mathbf{P}(t)$ enables the transfer of energy between frequency components of the field, such as the generation of a second-harmonic wave at frequency $2w$ from a fundamental wave at w. Thus, the nonlinear polarization is the physical mechanism that underlies all nonlinear optical phenomena.

The nonlinear dependence of the polarization can be justified intuitively from a classical anharmonic oscillator model. In this picture, an electron bound to an atom experiences a restoring force that is not strictly proportional to its displacement. The polarization, proportional to the average displacement of these charges, therefore acquires higher-order terms in the applied field. These additional terms correspond to field-dependent susceptibilities $\chi^{(n)}$, which may be treated as tensors to account for coupling between orthogonal field components. For simplicity, and because most experiments in this work employ linearly polarized light in isotropic media, the scalar form of Eq. (6.2) suffices to describe the relevant effects. Under the assumption of an instantaneous response, valid for electronic nonlinearities occurring on sub-femtosecond timescales, the susceptibilities $\chi^{(n)}$ can be considered real constants, independent of time and frequency. This approximation neglects dispersion and losses but adequately describes the behavior of transparent materials under nonresonant excitation. For condensed matter, typical magnitudes of the nonlinear susceptibilities are extremely small compared with the linear term. For instance, Boyd [34] estimates

$$\chi^{(2)} \sim 10^{-12}\ \mathrm{m/V}, \qquad \chi^{(3)} \sim 10^{-24}\ \mathrm{m^2/V^2},$$

which implies that electric fields of 10^7–10^8 V/m (intensities of 10^{10}–10^{12} W/m^2) are required for observable nonlinear effects. Such field strengths are readily achieved with laser beams focused to micrometer-scale waists, where the local intensity is high enough to induce measurable nonlinear refractive index changes. Finally, from a phenomenological standpoint, the nonlinear polarization term $\mathbf{P}^{(3)}(t) = \epsilon_0 \chi^{(3)} |\mathbf{E}(t)|^2 \mathbf{E}(t)$ produces an intensity-dependent refractive index,

$$n(I) = n_0 + n_2 I, \tag{6.4}$$

where the nonlinear refractive index n_2 is related to $\chi^{(3)}$ by

$$n_2 = \frac{3}{4 n_0^2 \epsilon_0 c} \mathrm{Re}[\chi^{(3)}]. \tag{6.5}$$

This relation links a directly measurable macroscopic parameter (n_2) to the microscopic electronic response ($\chi^{(3)}$), forming the theoretical foundation for experimental techniques such as the Z-scan. Yet, the quantitative determination of nonlinear coefficients such as n_2 and $\chi^{(3)}$ crucially depends on the accurate evaluation of the optical intensity at the sample, given by

$$I_0 = \frac{2P_0}{\pi w_0^2}, \tag{6.6}$$

where P_0 is the beam power and w_0 is the beam waist. Because $I_0 \propto 1/w_0^2$, even a small uncertainty in the beam waist produces a large uncertainty in the estimated intensity and therefore in the derived nonlinear coefficients. For instance, a 5% error in w_0 results in a 10% deviation in I_0, which propagates directly to the measured value of n_2. This dependence establishes the motivation for precise and automated beam profiling methods such as the knife-edge technique employed in this work to ensure accurate nonlinear optical characterization.

6.2 Third-Order Nonlinear Optical Phenomena

In centrosymmetric media, the even-order nonlinearities vanish because the material response must remain invariant under spatial inversion. As a result, the dominant nonlinear term is of third order, and the induced polarization is given by

$$\mathbf{P}^{(3)}(t) = \epsilon_0 \chi^{(3)} \mathbf{E}^3(t), \tag{6.7}$$

where $\chi^{(3)}$ is the third-order nonlinear susceptibility. Media that exhibit this kind of response are commonly referred to as Kerr media [1]. The third-order nonlinearity gives rise to a wide variety of parametric processes such as third-harmonic generation (THG), self-phase modulation (SPM), four-wave mixing (FWM), and the optical Kerr effect.

6.2.1 Third-Harmonic Generation and Kerr Effect

When a monochromatic optical field $\mathbf{E}(t) = E_0 \cos(\omega t)$ is applied to a third-order medium, the nonlinear polarization contains terms oscillating both at the fundamental and at three times the frequency of the excitation [34]:

$$\mathbf{P}^{(3)}(t) = \frac{3}{4}\epsilon_0 \chi^{(3)} E_0^3 \cos(\omega t) + \frac{1}{4}\epsilon_0 \chi^{(3)} E_0^3 \cos(3\omega t). \tag{6.8}$$

The first term corresponds to a modification of the medium's refractive index at the same frequency as the incident wave, leading to an intensity-dependent refractive index, while the second term represents the generation of a new field at 3ω, known as third-harmonic generation (THG). Although THG is often weak compared to second-harmonic generation, it plays an important role in frequency conversion and ultrafast diagnostics. More relevant to the present work is the first term of Eq. (6.8), which gives rise to a nonlinear contribution to the refractive index described by

$$n(I) = n_0 + n_2 I, \tag{6.9}$$

where n_2 is the nonlinear refractive index coefficient, related to the susceptibility $\chi^{(3)}$ by

$$n_2 = \frac{3}{4n_0^2 \epsilon_0 c} \mathrm{Re}[\chi^{(3)}]. \tag{6.10}$$

This phenomenon is known as the optical Kerr effect, and it manifests as a self-induced change in the refractive index proportional to the local light intensity. Physically, this means that the phase velocity of a wave depends on its own amplitude, leading to a variety of nonlinear propagation effects, including self-phase modulation and self-focusing [1], [34]. Typical values of n_2 range from 10^{-16} to 10^{-14} cm^2/W in glasses, up to 10^{-10} cm^2/W in semiconductors, depending on wavelength and polarization [1].

6.2.2 Self-Phase Modulation and Self-Focusing

As a light beam propagates through a Kerr medium, the spatially varying intensity profile $I(r, z)$ induces a corresponding refractive index distribution $n(I)$. This produces a phase shift that depends on the beam's own intensity, an effect known as self-phase

modulation (SPM). The accumulated phase shift after a propagation distance L is given by

$$\Delta\phi = k_0 n_2 I_0 L, \tag{6.11}$$

where I_0 is the peak intensity at the beam center and $k_0 = 2\pi/\lambda$. If the refractive index increases with intensity ($n_2 > 0$), the central region of the beam, being more intense, experiences a higher refractive index than the periphery. Consequently, the phase fronts curve inward and the beam self-focuses, as shown schematically in Fig. 6.1. This self-focusing effect can further enhance the local intensity, making it a crucial mechanism in nonlinear optical interactions and a limiting factor in laser damage [34].

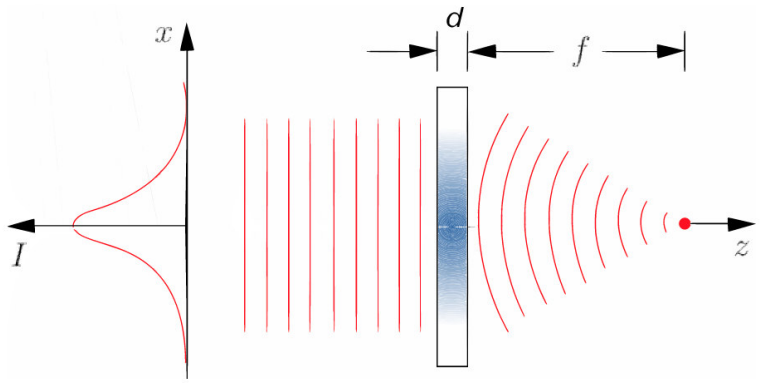

FIGURE 6.1: Schematic illustration of self-focusing due to the optical Kerr effect. The refractive index profile mimics the beam intensity distribution, producing a lens-like effect that increases the local field amplitude.

The interplay between self-phase modulation and diffraction determines whether a beam will self-focus, self-trap, or diverge. The critical power for self-focusing is approximately

$$P_{\text{cr}} = \frac{\alpha_0 \lambda^2}{4\pi n_0 n_2}, \tag{6.12}$$

where α_0 is a numerical factor that depends on the beam profile ($\alpha_0 = 1.8962$ for a Gaussian beam). For power levels above P_{cr}, self-focusing dominates over diffraction.

6.2.3 Experimental Relevance and Dependence on Beam Waist

From an experimental point of view, the accurate determination of the nonlinear refractive index n_2 requires a precise knowledge of the beam intensity at the sample, since the measured nonlinear phase shift depends linearly on I_0. The on-axis intensity of a Gaussian beam is given by

$$I_0 = \frac{2P_0}{\pi w_0^2}, \tag{6.13}$$

where P_0 is the beam power and w_0 the beam waist. Therefore, any uncertainty in w_0 propagates quadratically to I_0 and directly to n_2, since $n_2 \propto 1/I_0$. For this reason, the experimental precision in measuring w_0 is not a secondary consideration, it fundamentally determines the accuracy of all derived nonlinear parameters, including n_2 and $\chi^{(3)}$. In techniques such as Z-scan, where the nonlinear refractive index is retrieved

from transmittance variations as a function of axial position, the dependence of I_0 on w_0 makes beam characterization a critical step in obtaining reliable nonlinear coefficients. The methodology presented in this work therefore focuses on the development of an automated and highly repeatable knife-edge system for the precise measurement of w_0, providing a robust foundation for subsequent nonlinear optical characterization and validation of theoretical models based on the third-order susceptibility.

6.3 Nonlinear optics applications

Accurate knowledge of the beam waist w_0 and its propagation parameters is not only fundamental for Gaussian beam characterization, but also crucial for a wide variety of nonlinear optical experiments. In most cases, the relevant physical quantities depend explicitly on the on-axis intensity

$$I_0 = \frac{2P}{\pi w_0^2}, \tag{6.14}$$

so any uncertainty in the waist determination translates directly into errors in the estimation of nonlinear coefficients or efficiencies. In practice, the primary source of error in many nonlinear optical measurements is often the uncertainty in the laser beam's fluence or intensity profile (i.e. the beam shape and size). Accurate determination of parameters like the nonlinear refractive index n_2 or the two-photon absorption coefficient β thus depends critically on how precisely the laser source is characterized in terms of its spatial profile (beam waist), temporal profile, and power/energy stability [37].

6.3.1 Z-scan Technique

The Z-scan method is one of the most widely used techniques for measuring the nonlinear refractive index n_2 and the third-order susceptibility $\chi^{(3)}$ of optical materials [36]. It relies on translating the sample through the focus (along the propagation axis) and recording the transmitted intensity through a finite aperture. The normalized transmittance curve depends explicitly on the beam waist and Rayleigh range:

$$T(z) \propto \frac{\Delta\phi_0}{1 + (z/z_R)^2},$$

where $\Delta\phi_0 = kn_2 I_0 L_{\text{eff}}$ is the on-axis nonlinear phase shift. Since $I_0 \propto 1/w_0^2$, even small uncertainties in w_0 can lead to significant deviations in the retrieved value of n_2. Indeed, a major source of error in Z-scan measurements is the uncertainty in the beam's assumed profile and peak intensity. Discrepancies of up to one order of magnitude have been reported in literature values of n_2, partly due to inconsistent beam waist characterization [1].

6.3.2 Nonlinear Absorption and Multiphoton Processes

In open-aperture Z-scan and multiphoton absorption experiments, the nonlinear absorption coefficient β is derived from the transmitted intensity as a function of input intensity. Since $I_0 \propto 1/w_0^2$, errors in waist measurement propagate quadratically into the estimation of β. For example, a 5% error in beam radius leads to a 10% error in peak

intensity, which results in 20% error in the extracted β. Accurate beam waist knowledge is therefore critical for evaluating two-photon and higher-order absorption coefficients [37].

6.3.3 Kerr Effect and Self-Focusing

The Kerr effect induces an intensity-dependent refractive index change, which can cause self-focusing when the beam power exceeds a critical value. For a Gaussian beam, the critical power is given by [39]:

$$P_{\text{cr}} \approx \frac{3.77\lambda^2}{8\pi n_0 n_2}.$$

Although this expression is independent of w_0, the experimental identification of collapse thresholds depends on knowing the beam waist accurately, since intensity distributions are calculated from I_0. In filamentation experiments, the ratio P/P_{cr} determines whether stable filaments form or multiple filamentation occurs [40]. Thus, waist uncertainty directly impacts the interpretation of Kerr-induced self-focusing.

Chapter 7

Methodology

7.1 Laser Warm-up and Initial Alignment

The 543.5 nm He-Ne laser was turned on and allowed to thermally stabilize for approximately 30–45 minutes. Initial beam alignment was performed using a diaphragm placed near the laser aperture and a set square positioned directly on the optical table. The diaphragm served to define the beam's central axis, while the set square was used to verify the beam height at two axial positions along the propagation path. Manual tilt adjustments were applied to the laser mount until the beam spot maintained a constant vertical position across both reference points, ensuring collinearity of the beam with the optical table. Once the beam path was verified to be collinear and stable, the diaphragm was removed, and the system was deemed ready for the knife edge scans.

7.2 Knife-edge Tests: Blade Rotation

For the first set of tests, once the laser beam was aligned, the knife-edge was mounted on its translation platform at an initial distance of 23.5 cm from the laser aperture, with the detector positioned at 46 cm, aligned to the beam spot height. Each dataset consist on ten transverse scans of the knife-edge, with an axial step size (z) of 10 mm and a transverse step size of 0.1 mm across 11 positions.

Reference measurements were first acquired with the blade oriented perpendicularly to the propagation axis. In total, 18 reference datasets were collected over two different days under comparable experimental conditions. Subsequently, the knife-edge was rotated by 15° to the right and left, yielding 12 datasets each over two days. Finally, the knife-edge was rotated by 45° to the left and to the right, for which 5 datasets were obtained in each case. For every transverse cut, the transmission curves were fitted to extract the coefficients r_0, w, and P_0, corresponding to the beam center position, the beam radius, and the maximum transmitted power, respectively (see Sections 8.1.1, 8.1.3, and 8.1.4). These fitted parameters were then analyzed to evaluate the effect of knife-edge rotation on the beam characterization results. In addition, a second experimental stage, here referred to as the *validation platform* was later incorporated to assess the origin and impact of the curvature observed in the fitted beam-center trajectories $r_0(z)$ (see Section 8.1.2). These tests were designed to determine whether the slight nonlinearity detected in the baseline measurements was an intrinsic mechanical signature of the translation system or a consequence of residual misalignment.

7.3 Knife-edge Tests: Beam Misalignment

In this case, the initial configuration between the laser aperture, the knife-edge, and the detector was preserved as in the first set of tests. A total of 12 reference measurements were recorded under aligned conditions with the knife-edge oriented transversely to the beam propagation. Subsequently, controlled severe misalignments were introduced by deliberately displacing the detector from its original aligned position in four different directions: 2 cm upward, 2 cm downward, 3 cm to the right, and 3 cm to the left. In the vertical displacements, the knife-edge was also shifted by 10 mm to preserve the sigmoidal shape of the transmission curves. For each misalignment orientation, five datasets were collected, allowing comparison with the aligned reference measurements (see Section 8.2). To further examine the influence of platform mechanics on the alignment analysis, additional measurements were performed using the *validation platform* (see Section 8.2.1).

7.4 Knife-edge Beam Profiling with Focusing Lens

A converging lens with a focal length of approximately 15 cm was inserted between the laser aperture and the knife-edge to focus the beam. Alignment was performed manually by minimizing the back-reflections from the lens. In this case, different experimental configurations were employed to evaluate the repeatability of the measurements under varying conditions. In the first configuration, the distances relative to the laser aperture were: 3 cm to the lens, 10 cm to the initial knife-edge position, and 35.5 cm to the detector. Transverse scans were carried out with step sizes of 0.03 and 0.05 mm. In the second configuration, the distances were: 14 cm to the lens, 21 cm to the knife-edge, and 46 cm to the detector. Here, the transverse step size varied among 0.1, 0.03, and 0.05 mm. Knife-edge measurements were performed by scanning the region near the lens focal point, covering axial positions between approximately 15 and 40 mm. Transverse scans were acquired with axial step sizes (z) between 3 and 5 mm.

For each transverse cut, the transmitted power was fitted using Eq. (5.3) to extract the parameters $r_0(z)$, $w(z)$, and $P_0(z)$. The evolution of these parameters was analyzed to evaluate the beam alignment using metrics such as the standard deviation σ_{r_0}, the normalized deviation σ_{r_0}/w_0, the slope of the linear regression of $r_0(z)$, and the coefficient of determination R^2 (see Section 8.3). In this study, a beam was considered well aligned when $\sigma_{r_0}/w_0 < 0.01$ and $|dr_0/dz| < 0.02\mu\text{m/mm}$, with a corresponding $R^2 > 0.95$, while $\sigma_{r_0}/w_0 < 0.05$ was still regarded as acceptable alignment. Finally, the retrieved beam width $w(z)$ was fitted to the hyperbolic model of Gaussian beam propagation, Eq.(5.4), in order to obtain the waist parameters w_0, z_0, and z_R.

Chapter 8

Results

This chapter presents and discuss the results obtained from the three experimental cases described previously. For each set of data, comparative analyses are provided to assess reproducibility between different translation platforms, as well as the consistency of measurements performed on the same platform across different days. Although a comprehensive reproducibility study was not pursued, the selected datasets are representative and allow clear interpretation of the main tendencies of the estimated parameters.

The decision to employ both a baseline platform and a validation platform originated from an unexpected observation during the experimental phase: the fitted beam-center trajectories, $r_0(z)$, exhibited a nonlinear curvature along the propagation axis, contrary to theoretical expectations for a well-aligned Gaussian beam, where $r_0(z)$ should follow a linear trend with nearly zero slope. At that stage, it was unclear whether this curvature reflected actual beam misalignment or mechanical artifacts inherent to the translation system. To investigate this behavior, additional measurements were conducted using various wavelengths on the baseline platform, followed by tests on a second, mechanically identical translation system referred to as the validation platform. The comparison revealed that all measurements acquired with the same platform exhibited a consistent curvature in $r_0(z)$, regardless of wavelength or optical alignment. This finding confirmed that the observed nonlinearity was primarily of mechanical origin, likely due to small stage's intrinsic straightness deviation or guide rail runout. This result led to a re-evaluation of how alignment and power stability analyses were performed. The recognition of this mechanical contribution prompted the development of new diagnostic metrics. Consequently, the datasets presented in this chapter were designed to replicate controlled yet adverse alignment conditions, allowing the robustness of the proposed method and metrics to be tested under realistic experimental perturbations. These analyses provide valuable insight into the stability, sensitivity, and tolerance of the knife-edge technique when applied to practical beam characterization scenarios.

8.1 Rotated knife results

In this first stage of the methodology, the knife-edge technique was applied under different rotation angles and reference conditions to validate the working hypothesis that the evolution of the fitted coefficients r_0, w, and P_0 act as indicators of beam alignment and stability.The beam parameters were extracted from the nonlinear least-squares fitting procedure described in Chapter 3.1.2. To establish a reference, several scans were performed with the knife edge aligned perpendicular to the propagation axis. These

measurements serve as the control case against which rotated configurations are compared. By contrasting the obtained parameters with these references, it is possible to quantify the influence of blade orientation on the estimation of the beam trajectory and to evaluate the robustness of the measurement. By perturbing the ideal conditions of the experiment, we simulate controlled errors and quantify their impact on the estimated beam parameters.

The following figures summarize the reference case and the rotated knife-edge measurements. Each curve represents the mean of multiple repeated scans, while vertical error bars denote the standard deviation across repeats, reflecting the dispersion of the acquired data. Different markers are used to distinguish each measurement, and the color scheme identifies the experimental condition: red traces correspond to scans where the knife was rotated to the right, blue to those rotated to the left, and black to the reference configurations. The subscript notation indicates the platform used for acquisition: measurements labeled with the subscript $_{B}$ were obtained with the baseline platform, while those with $_{V}$ correspond to the validation platform. In all cases, dashed black lines represent the uncorrected (raw) polynomial fits, whereas the solid black lines show the corrected linear trend obtained after curvature compensation. This consistent color and symbol coding will be maintained throughout the remainder of this section to facilitate comparison between configurations and to highlight reproducibility across experimental platforms.

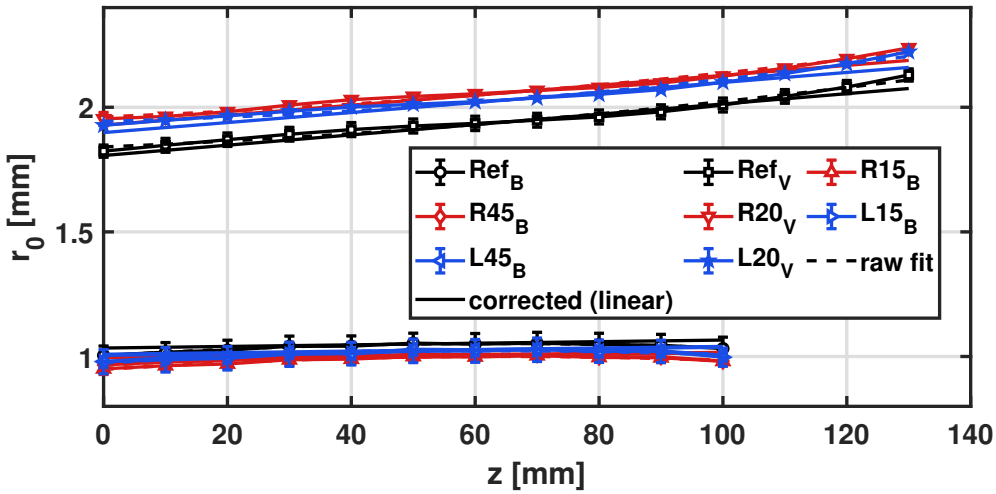

FIGURE 8.1: Beam center position $r_0(z)$ obtained for different reference and rotated knife-edge conditions.Two distinct reference levels can be observed, corresponding to measurements acquired with different translation stages (baseline vs. validation).

In Figure 8.1, two distinct bundles of trajectories are evident, corresponding to measurements performed with the baseline and validation translation platforms under different experimental configurations. Within each platform, the results are consistent across repeated acquisitions. The vertical separation between these bundles is expected since the setups were not intended to reproduce identical alignment or geometric conditions (Nonetheless, reproducing comparable conditions is feasible if strict repeatability tests are required). Across the full axial window (0–130 mm), the $r_0(z)$ traces for both

platforms follow a smooth, nearly linear trend with small, systematic offsets of about 0.8–1.1 mm between bundles. A closer inspection reveals that the reference trajectories (black symbols) are not perfectly linear with z, as predicted by ideal beam propagation theory, but instead show a subtle upward curvature. Interestingly, this curvature is reproduced by all rotated-knife traces regardless of the platform or orientation.Within each group, the individual traces (associated with different blade rotations) remain consistent with one another and exhibit low dispersion, as shown by the small standard deviation bars (below 0.05 mm). This confirms that the differences between datasets originate primarily from platform-dependent mechanical factors rather than random fluctuations. The fact that both the baseline and validation datasets share the same curvature indicates that this feature is not an optical or alignment artifact but rather an inherent mechanical signature of the translation stages. The fitted slopes for the baseline platform range between 0.21 and 0.36 μm/mm, while those for the validation platform (labeled 'V') fall between 1.9 and 2.1 μm/mm. These values remain stable across the different rotation angles, reflecting a robust and reproducible behavior within each mechanical configuration. The preservation of the curvature and slope magnitude across repetitions reinforces the interpretation that both systems exhibit consistent yet platform-specific mechanical trends, validating the reliability of the automated acquisition method.

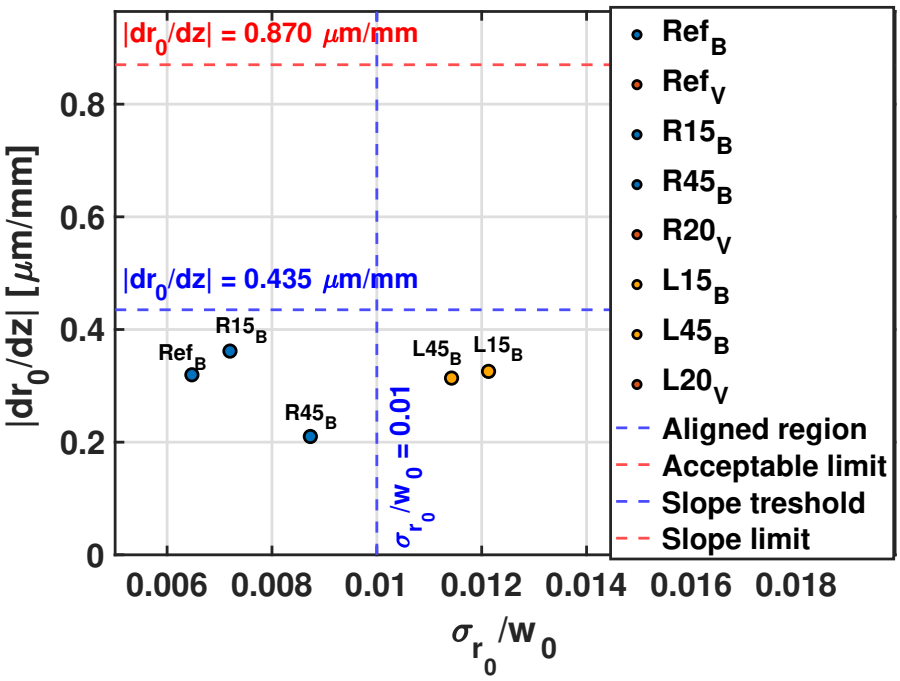

FIGURE 8.2: Alignment metrics derived from the fitted beam-center trajectories $r_0(z)$, showing the normalized dispersion σ_{r_0}/w_0 versus the absolute slope $|dr_0/dz|$. Vertical error thresholds (blue) correspond to the alignment limits based on the beam-centering dispersion, while horizontal dashed lines (red) represent slope tolerances. Points are colored according to alignment quality.

To further quantify the alignment quality across all experimental conditions, the metrics derived from the fitted $r_0(z)$ curves were condensed into an alignment map (Figure 8.2). Each point in this diagram represents a measurement condition, characterized by its normalized beam-center dispersion σ_{r_0}/w_0 and the fitted slope $|dr_0/dz|$, both extracted from the data presented in Figure 8.1. This representation provides a compact visual summary of alignment stability: the horizontal axis reflects the repeatability of the beam center (sensitivity to noise and mechanical jitter), whereas the vertical axis captures the systematic drift of r_0 along z, mainly influenced by the stage straightness or tilt. The blue and red dashed lines mark the adopted tolerance thresholds. **Following the revised criteria for the no-lens configuration, a beam is considered *well aligned* when $\sigma_{r_0}/w_0 < 0.01$ and $|dr_0/dz| < 0.435\mu$m/mm, and *acceptably aligned* when $\sigma_{r_0}/w_0 < 0.05$ and $|dr_0/dz| < 0.870\mu$m/mm.** These limits correspond to cumulative beam-center drifts of $0.25, w_0$ and $0.5, w_0$, respectively, across the 130 mm scanning range, and were selected to reflect the mechanical tolerances and beam size typical of the unfocused configuration $w_0 \approx 400\mu$m. Under these criteria, all baseline measurements fall comfortably within the acceptable region, with σ_{r_0}/w_0 typically below 0.012 and slopes ranging between 0.21 and 0.36 μm/mm, consistent with good mechanical straightness of the translation stage. In contrast, the validation platform yields larger slopes (1.9–2.1 µm/mm), indicating an increased mechanical curvature that dominates the axial trend. Therefore, the alignment map not only validates the internal consistency of the $r_0(z)$ fits but also highlights the distinct mechanical signatures of each translation system.

Results extracted from the polynomial fits of $r_0(z)$ provide further insight into the alignment stability summarized in Figure 8.2. For the baseline platform, the fitted slopes range between 0.21 and 0.36μm/mm with residual dispersions σ_{r_0} between 2.7 and 5μm, corresponding to normalized deviations σ_{r_0}/w_0 below 0.012. These values confirm that all baseline configurations remain well within the "aligned" or "minor misalignment" regions. In contrast, the validation platform exhibits slopes of approximately 2μm/mm and dispersions of 11–12.5μm, producing normalized deviations of 0.028–0.031, which place those measurements firmly in the "significant misalignment" zone. The fitted curves consistently yield high linearity ($R^2 > 0.90$ for all baseline cases and up to 0.98 for the validation ones), with the quadratic curvature terms ($\pm$0.02–0.03μm/mm^2) indicating a mild, platform-dependent mechanical bow rather than optical distortion. The minimal difference between raw and corrected fits (ΔRelError $\approx 10^{-17}$, ΔSlope $\approx 10^{-15}$) confirms that the centering correction procedure introduces negligible bias, validating the robustness of the analysis pipeline. Overall, these quantitative results reinforce the classification derived from the alignment map: the baseline platform maintains stable alignment across all rotations, while the validation setup exhibits consistent, geometry-induced drift.

In Figure 8.3, the separation between platforms is less pronounced than in the $r_0(z)$ case, yet two bundles can still be discerned, consistent with the use of different translation stages and operating conditions. Across the entire axial range, the rotated-knife traces lie very close to, and in several segments overlap with, the reference curves within the error bars. This behavior confirms the robustness of the fitting procedure for retrieving $w(z)$ even when the blade orientation is perturbed. For both platforms, the retrieved

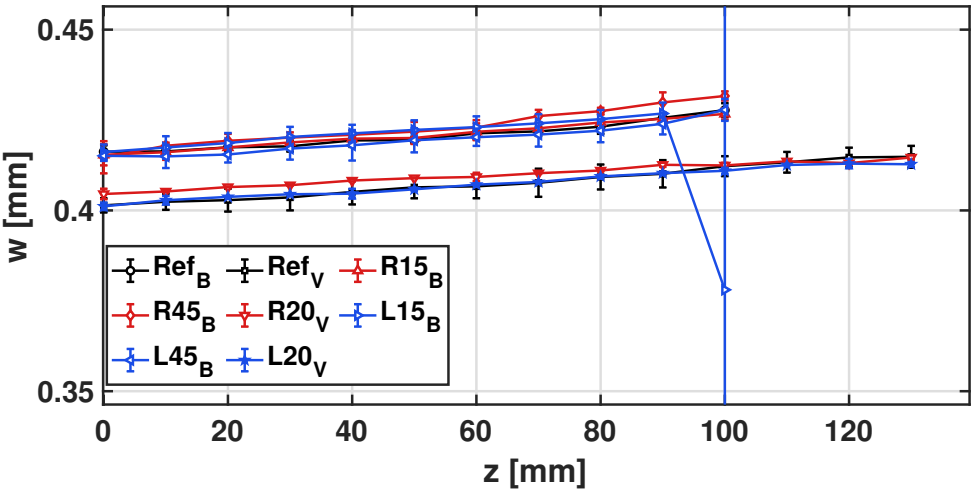

FIGURE 8.3: Beam radius $w(z)$ as a function of propagation distance for the same set of conditions. The radius remains stable across repetitions, with only minor variations observed in the case of the 20° and 45° rotations. The dispersion reflects the sensitivity of the method to alignment and stage curvature.

beam radius increases slightly with z, exhibiting a positive slope of approximately 2–3μm/mm. This trend agrees with the expected diffraction-driven expansion of a Gaussian beam and remains nearly linear over the limited axial span explored (0–130 mm). In this range, the hyperbolic propagation law of the Gaussian beam can be well approximated by a linear function, as observed here. The absolute difference between the baseline and validation bundles remains below 0.02 mm across all positions, indicating that the apparent offset is small compared with the mean beam size $w \approx 0.41$–0.43 mm. A single isolated outlier is present at $z \approx 100$ mm in one of the left-rotated measurements, where the estimated w value deviates significantly from the local trend. Such anomalies are occasionally observed in knife-edge measurements and may arise from transient laser power fluctuations, mechanical stick–slip or backlash of the translation stage, minor imperfections on the blade edge, or temporary environmental perturbations. The point is retained in the plot for completeness and to illustrate the typical variability of the method under realistic laboratory conditions. A detailed per-platform analysis will be provided later in this section to quantify these effects.

In Figure 8.4, all traces cluster within a narrow absolute range (1.50–1.54 mW) yet exhibit comparatively larger scatter than the other fitted parameters, making $P_0(z)$ the most sensitive metric to blade orientation in this study. Each rotated condition shows a clear offset relative to the reference curves, consistent across the entire z-range, which indicates a systematic, angle-dependent effect rather than random fluctuations. The validation platform ($P_{0,\mathrm{V}}$) generally displays slightly smaller dispersion than the baseline platform ($P_{0,\mathrm{B}}$); however, this difference should be interpreted with caution, as the validation bundle includes fewer repeated measurements. Even so, the persistence of the angle specific offsets across both platforms confirms that geometry rather than sample size dominates the observed variability. The typical standard deviation within each trace is around 10–15μW, representing less than 1% of the mean optical power. The

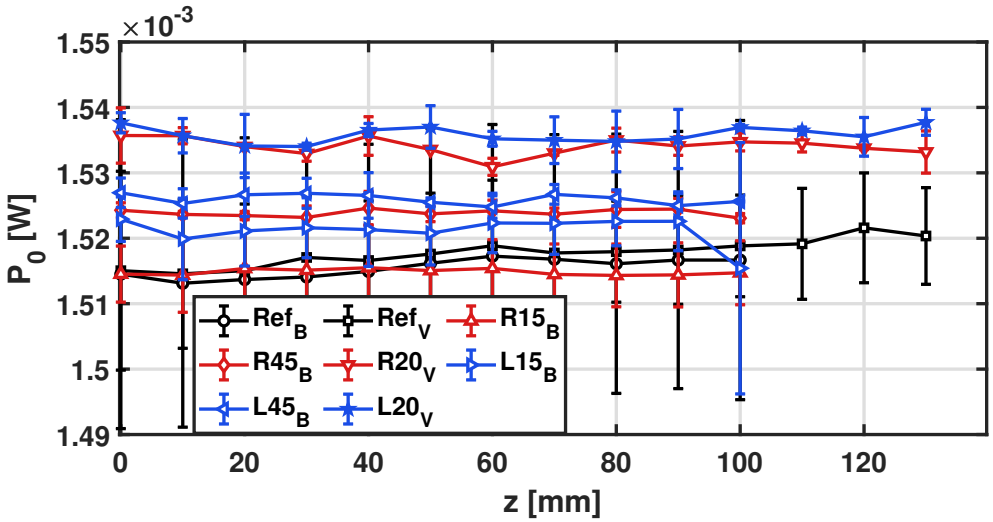

FIGURE 8.4: Maximum transmitted power $P_0(z)$ retrieved from the knife-edge fits. The power remains nearly constant with propagation, confirming that the detected variations are primarily due to beam geometry rather than source fluctuations. Small offsets between platforms again highlight mechanical differences in the displacement systems.

systematic offsets between different blade orientations, on the other hand, reach up to 25–30μW, corresponding to $\sim$2% relative shifts. These values are fully consistent with the expected changes in the intercepted optical fraction as the knife inclination modifies the effective overlap between the laser footprint and the detector's active area.

The blade rotation modulates the proportion of light reaching the detector through a combination of geometric projection, partial scattering along the edge, and small variations in reflection angle. These effects directly alter the estimated $P_0(z)$ even when the true beam power remains constant, explaining both the increased dispersion and the orientation-dependent offsets observed. In most rotated cases, the mean retrieved P_0 is slightly higher than for the strictly transverse blade, consistent with a reduced effective occlusion at nonzero angles. Consequently, $P_0(z)$ cannot be considered a stable quantitative indicator of beam alignment under rotation. In the following analysis, $r_0(z)$ and $w(z)$ are therefore adopted as the primary alignment diagnostics, while $P_0(z)$ serves as a qualitative consistency check to verify the integrity of the power measurement throughout the scan.

8.1.1 Reproducibility and cross-platform comparison

In this subsection we assess cross-platform reproducibility between the baseline platform (primary stage used during development) and the validation platform (introduced subsequently to verify unexpected findings). For each rotated condition, repeated scans were averaged to obtain a mean trajectory, and vertical error bars represent the across-repeat standard deviation (SD). Methodologically, all comparisons are performed over the common axial grid defined by the intersection of the z positions in each pair, avoiding interpolation bias. Most pairs involve different blade angles; the only angle-matched case is the reference pair. Table 8.1 summarizes cross-platform agreement by comparing

the mean curves across repeats. We report the mean absolute error (MAE) and the root-mean-square error (RMSE) in absolute units (μm for r_0 and w, μW for P_0), together with the Pearson correlation coefficient (ρ) and the coefficient of determination (R^2). Outliers are retained to reflect the full variability of the measurements; consequently, the quoted figures capture both random fluctuations and geometry-driven systematics.

TABLE 8.1: Cross-platform comparison (baseline vs. validation) over the common z grid. Units: μm for r_0, w; μW for P_0. Note: angle mismatch applies to all rows except *Refs vs. refs_p*.

Pair	MAE(r_0)	MAE(w)	RMSE(P_0)	$R^2_{r_0}$	R^2_w	$R^2_{P_0}$	ρ_{r_0}
Refs vs. refs_p	881.11	14.42	1.70	0.476	0.969	0.832	0.690
R15 vs. R20_p	1051.80	12.03	19.34	0.520	0.978	0.157	0.721
L15 vs. L20_p	1002.70	17.35	14.72	0.376	0.073	0.099	0.613
R45 vs. R20_p	1043.30	14.24	10.33	0.266	0.960	0.038	0.516
L45 vs. L20_p	998.59	13.35	9.74	0.378	0.916	0.006	0.615

The most consistent behavior is observed for the beam radius $w(z)$. For the reference pair (as expected due to angle mismatch), the agreement is strong, with $R^2_w = 0.969$ and MAE$(w) = 14.4\mu$m. When the blade angles differ, the good performance largely persists: R^2_w remains high (0.916–0.978) and the absolute deviations stay in the 12–17 μm range. An apparent exception is the L15 vs. L20_p comparison, where $R^2_w = 0.073$ coexists with a modest MAE$(w) = 17.4\mu$m; this reflects a small dynamic range coupled with a slight offset that depresses R^2 without implying practically relevant errors for alignment.In contrast, the beam center $r_0(z)$ exhibits large absolute differences across platforms (MAE $\approx$ 0.88–1.05 mm) and only moderate determination coefficients (0.27–0.52 for mismatched-angle pairs; 0.476 for the references). These discrepancies are consistent with platform-dependent offsets and mild stage curvature, rather than random noise.

Finally, the maximum power $P_0(z)$ is the least reproducible metric under angle mismatch: $R^2_{P_0} \ll 0.5$ with RMSE between 9.7 and 19.3 μW, in line with geometry-driven changes in effective interception. Even for the reference pair the agreement, while improved ($R^2_{P_0} = 0.832$, RMSE $= 1.70\mu$W), remains secondary compared with $w(z)$. Overall, the table confirms the robustness of $w(z)$ as a cross-platform indicator, underscores the need to register $r_0(z)$ before comparing platforms, and supports treating $P_0(z)$ as a qualitative consistency check rather than a primary alignment diagnostic.

8.1.2 On whether curvature removal improves alignment diagnostics

We consider that the metrics used so far, the normalized dispersion σ_{r_0}/w_0 and the linear slope $|\mathrm{d}r_0/\mathrm{d}z|$, are sufficient to describe and compare the datasets. To validate this choice, we tested a curvature–removal approach in which $r_0(z)$ is fitted with a second–order polynomial and the quadratic term is subtracted prior to re–estimating the linear trend. Two correction modes were evaluated: `ref`, which subtract the curvature from the baseline reference scan, and `self`, where the curvature is estimated from the dataset itself. It was found that:

- **Reference curvature degrades cross-platform metrics (Table 8.2).** For the validation platform (rows labeled "V"), subtracting the *baseline* curvature:

- increases σ_{r_0}/w_0 by $+0.05$–$+0.06$ (absolute),
- inflates the slope by $\approx +0.38\mu\text{m/mm}$,
- and reduces R^2 by 0.07–0.10.

This is consistent with opposite curvature signs across platforms: the validation stage exhibits positive curvature $\left(+0.016\text{–}+0.021\ \mu\text{m/mm}^2\right)$, whereas the baseline stage shows *negative* curvature $\left(\approx -0.025\ \mu\text{m/mm}^2\right)$. Curvature is therefore platform–specific and not transferable.

- **Self curvature is neutral for alignment (Table 8.3).** Across all conditions, subtracting the own quadratic term leaves the alignment diagnostics essentially unchanged:
  - $\Delta(\sigma_{r_0}/w_0) \approx 0$,
  - Δ slope≈ 0 (slope reported in μm/mm),
  - and only negligible changes in R^2.

  This indicates that the quadratic coefficient captures a small, stable stage bow that does not affect either the linear trend or the residual spread relevant to alignment.

So far, a quadratic fit does not add actionable information for alignment in this dataset. The linear fit already captures the meaningful trend (slope), and σ_{r_0}/w_0 is insensitive to subtracting the quadratic term. In the remainder, we retain the linear analysis (slope and σ_{r_0}/w_0) as primary diagnostics and report the sign only as a mechanical descriptor of the translation stage.

TABLE 8.2: Effect of subtracting a reference curvature ('Ref') on $r_0(z)$. Values are shown as raw, corrected, and change (Δ = corr − raw). Units: slope in μm/mm; curvature sign from the raw quadratic fit.

Condition	Curv. sign	R^2_{raw}	R^2_{corr}	$\Delta(\sigma_{r_0}/wa_0)$	Δ slope [μm/mm]	Verdict
Ref_B	−	0.971	0.938	$+0.0000$	$+0.000$	Keep linear
R15_B	−	0.968	0.940	$+6.1\times10^{-6}$	$+0.000$	Keep linear
L15_B	−	0.908	0.820	$+1.1\times10^{-6}$	$+0.000$	Keep linear
R45_B	−	0.932	0.780	$+6.7\times10^{-6}$	$+0.000$	Keep linear
L45_B	−	0.913	0.825	$+7.5\times10^{-7}$	$+0.000$	Keep linear
Ref_V	+	0.980	0.904	$+0.051$	$+0.375$	Reject 'ref'
R20_V	+	0.982	0.903	$+0.052$	$+0.375$	Reject 'ref'
L20_V	+	0.983	0.882	$+0.062$	$+0.375$	Reject 'ref'

8.1.3 Baseline platform: parameter evolution analysis

We now focus on the baseline platform to examine parameter evolution in greater detail. For each rotation angle, $r_0(z)$ is modeled by a linear regression; $w(z)$ is compared against the reference trend and its local slope is reported; $P_0(z)$ is summarized by its mean and RMSE with respect to the reference. Residuals are inspected to detect systematic curvature or local defects.

TABLE 8.3: Self-curvature correction ('self') for $r_0(z)$. Alignment metrics remain unchanged within numerical precision. Units: slope in μm/mm; R^2 adimensional.

	σ_{r_0}/w_0			Slope [μm/mm]			R^2			Curv. sign
Condition	Raw	Corr	Δ	Raw	Corr	Δ	Raw	Corr	Δ	(raw)
Ref_B	0.00647	0.00647	0.00000	0.320	0.320	0.000	0.971	0.938	−0.033	−
$\mathrm{R15}_B$	0.00720	0.00720	0.00000	0.362	0.362	0.000	0.968	0.940	−0.028	−
$\mathrm{L15}_B$	0.01213	0.01213	0.00000	0.326	0.326	0.000	0.908	0.820	−0.088	−
$\mathrm{R45}_B$	0.00873	0.00873	0.00000	0.210	0.210	0.000	0.932	0.781	−0.151	−
$\mathrm{L45}_B$	0.01143	0.01143	0.00000	0.314	0.314	0.000	0.913	0.825	−0.088	−
Ref_V	0.03071	0.03071	0.00000	2.067	2.067	0.000	0.980	0.979	−0.001	+
$\mathrm{R20}_V$	0.02774	0.02774	0.00000	1.997	1.997	0.000	0.982	0.982	+0.000	+
$\mathrm{L20}_V$	0.02769	0.02769	0.00000	2.011	2.011	0.000	0.983	0.982	−0.001	+

In this section we analyze the rotation experiments acquired on the baseline platform and use the validation platform only as a cross-check to contextualize trends and magnitudes. For each rotated condition, repeated scans were averaged to obtain a mean trajectory; vertical error bars represent the across-repeat standard deviation (SD). Unless stated otherwise, comparisons are made over the common axial positions to avoid interpolation bias.

On the baseline stage, the retrieved $r_0(z)$ traces remain close to the corresponding reference while exhibiting systematic, angle-dependent offsets that persist across z. The average offset between the rotated and reference traces is on the order of 40–60μm, with a standard deviation between 10 and 20μm across repeats. A slight curvature is visible in the reference trace and is reproduced by all rotated cases, confirming that this feature originates from the mechanical straightness or runout of the translation stage rather than from the blade rotation itself. Right-rotated configurations tend to cluster below the reference level, while the left-rotated cases lie slightly above or between them, both sets converging toward the reference trajectory for larger z values. The measured slopes of the fitted linear trends range between 0.25 and 0.35μm/mm, consistent across all orientations, which indicates a stable axial evolution of the beam center over the scanned range. This behavior mirrors that observed in the cross-platform comparison: although the absolute offsets differ between stages, the axial progression of $r_0(z)$ remains coherent. The reproducibility of the curvature and the persistence of the orientation-dependent offsets confirm that the dominant contribution arises from systematic mechanical effects rather than random noise or fitting errors. Consequently, these results validate the baseline platform as a reliable reference for assessing alignment trends and for quantifying the residual sensitivity of r_0 to mechanical imperfections under controlled rotation.

The retrieved $w(z)$ curves, for the baseline platform, exhibit a stable, nearly linear increase over the scanned range (0–100 mm), consistent with the expected diffraction-driven divergence of a Gaussian beam. Across all rotated configurations, the traces overlap closely with the reference within the standard-deviation error bars, confirming that the beam radius estimation is robust under moderate blade rotation. The fitted slopes of $w(z)$ lie in the range of 1.5–2.5 $\times 10^{-4}$ mm/mm, corresponding to an expansion of about 20 μm across the entire scan window—well within the expected propagation behavior for a waist of $w_0 \approx 0.40$ mm and Rayleigh range $z_R \approx 15$ mm.

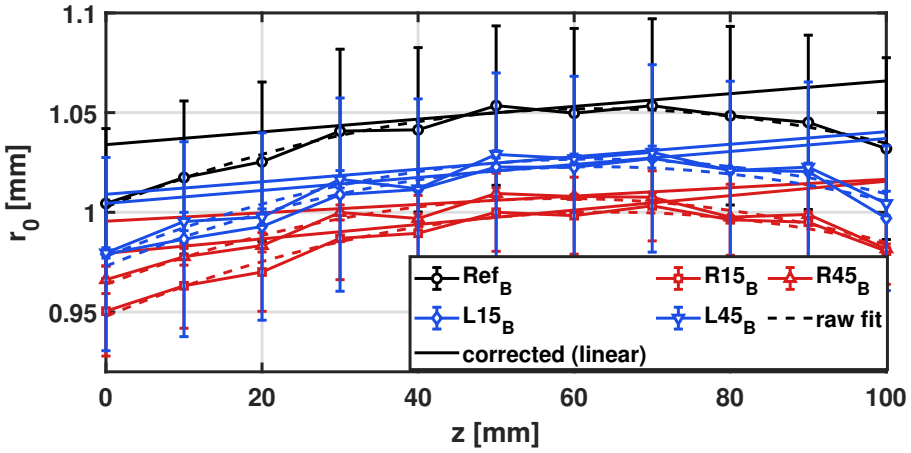

(A) Baseline platform: beam center $r_0(z)$ (mean $\pm$ SD).

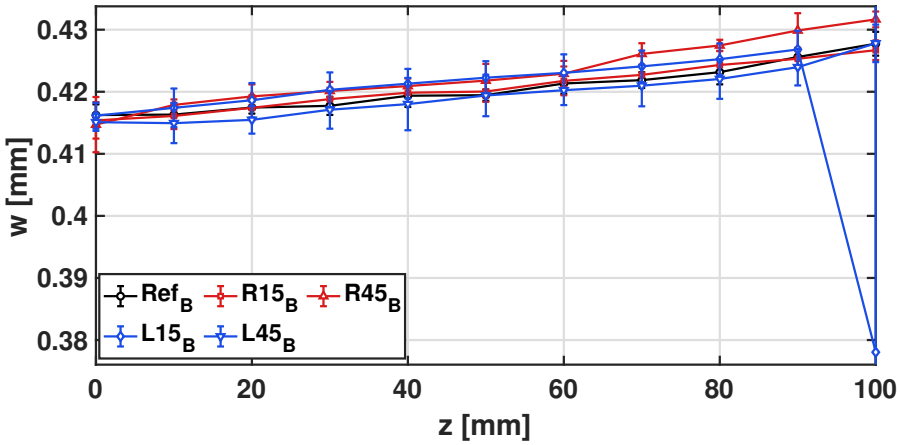

(B) Baseline platform: beam radius $w(z)$ (mean $\pm$ SD).

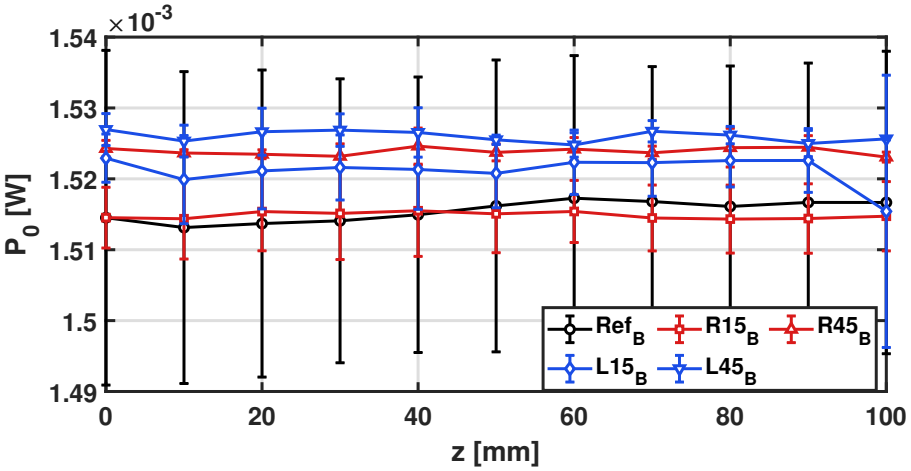

(C) Baseline platform: maximum power $P_0(z)$ (mean $\pm$ SD).

FIGURE 8.5: Baseline platform characterization: beam center $r_0(z)$, beam radius $w(z)$, and transmitted power $P_0(z)$ obtained from averaged and repeated knife-edge measurements.

A single outlier appears at the last axial position of the left-rotated 45° condition, where w drops abruptly. This deviation is isolated and not accompanied by similar behavior in neighboring points, suggesting a transient mechanical slip of the translation stage or a brief power fluctuation during acquisition rather than a systematic optical artifact. Notably, both the magnitude and pattern of this deviation are consistent with the minor irregularities observed in the validation stage, reinforcing that $w(z)$ is largely insensitive to blade orientation and inter-platform differences at the precision level relevant for alignment diagnostics. Overall, the results demonstrate that the beam-radius retrieval remains reliable and physically consistent even under deliberate perturbations of the knife-edge geometry.

$P_0(z)$ remains approximately constant for the baseline platform along the propagation axis, with mean values around $(1.51\text{–}1.53) \times 10^{-3}$ W and only small local fluctuations. Nonetheless, the traces exhibit clear, angle-dependent offsets and comparatively larger scatter across repeats, as evidenced by the wider error bars relative to those in $r_0(z)$ and $w(z)$. This behavior is expected: rotating the knife changes the fraction of the beam intercepted and the effective coupling into the detector's active area, slightly modifying the detected power even under constant incident intensity. The observed offsets are systematic for each angle and remain stable across z, confirming that they originate from geometry-dependent interception rather than random fluctuations. The validation platform shows the same qualitative behavior but with different offset magnitudes, which reinforces the conclusion that $P_0(z)$ is dominated by the mechanical and optical geometry of the setup rather than by noise or fitting uncertainty.

Quantitatively, the relative dispersion of P_0 is on the order of 0.5–0.7% across repeats, whereas r_0 and w vary by less than 0.1%. This contrast highlights the higher sensitivity of P_0 to edge inclination and detector alignment, confirming that it is not suitable as a primary alignment indicator. In this work, $P_0(z)$ is thus treated only as a qualitative consistency check, while $w(z)$ serves as the most stable figure of merit under rotation, and the dispersion and slope of $r_0(z)$ capture the underlying platform mechanics that can later be corrected through simple registration. Together, these parameters provide a complete picture of the system's stability and allow meaningful comparison between platforms and experimental days, as discussed in the next subsection. In the following subsection, we examine baseline reproducibility under nominally identical settings acquired on different days to assess day-to-day stability.

8.1.4 Same angle measurements acquired on different days

Day to day reproducibility was assessed on the baseline platform by repeating the reference and $\pm 15°$ configurations on two different days (labeled B_1 and B_2). For each case, repeated scans were averaged over a common axial grid ($K = 10\text{–}11$ points), and vertical error bars represent the across-repeat standard deviation. As shown in Figure 8.6a, the general behavior of $r_0(z)$ is well preserved from one session to another: the traces remain parallel and maintain their characteristic curvature and separation, reflecting the same platform-dependent mechanical signature observed previously.

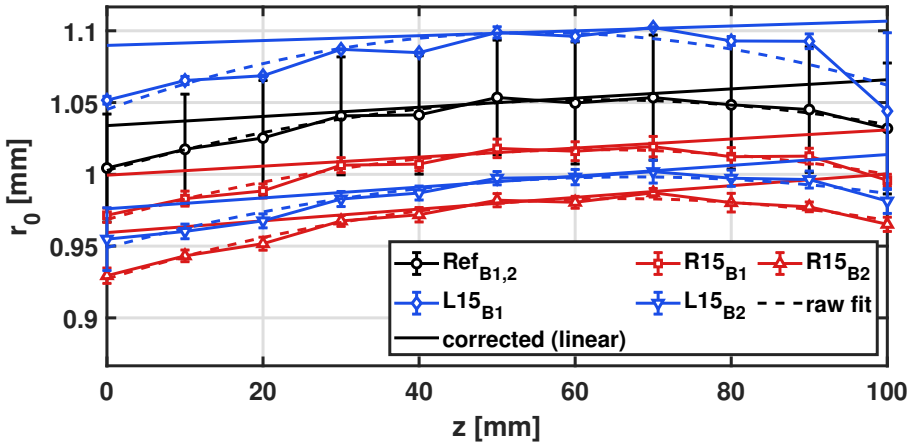

(A) Baseline platform: beam center $r_0(z)$ (mean $\pm$ SD).

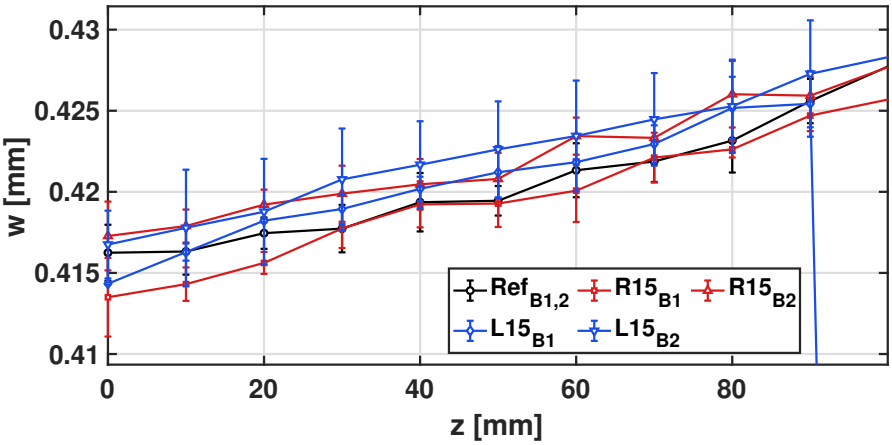

(B) Baseline platform: beam radius $w(z)$ (mean $\pm$ SD).

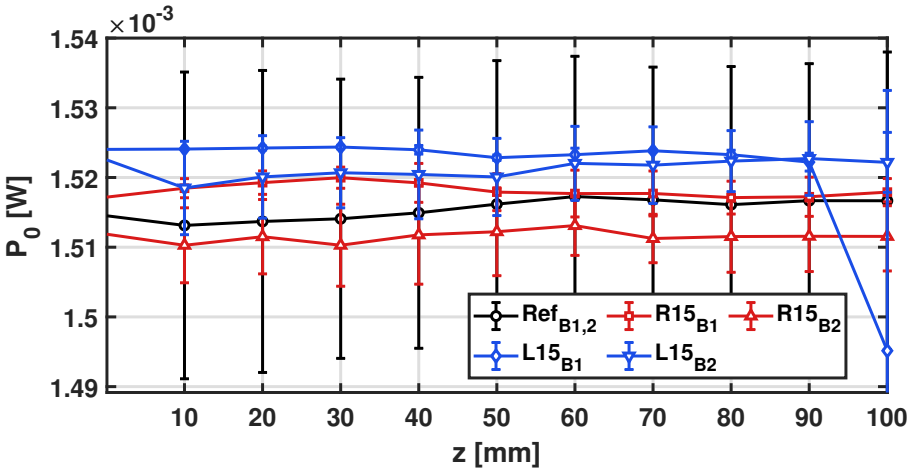

(C) Baseline platform: maximum power $P_0(z)$ (mean $\pm$ SD).

FIGURE 8.6: Consolidated comparison of the baseline platform: beam center $r_0(z)$, beam radius $w(z)$, and maximum power $P_0(z)$ obtained from repeated knife-edge measurements.

The alignment metrics remain within the "acceptable" region defined earlier. For the reference condition, the fitted slopes are $|dr_0/dz| = 0.469$ and 0.496μm/mm, with normalized dispersions $\sigma_{r_0}/w_0 = 0.021$ and 0.023, corresponding to stable alignment near the lower tolerance boundary. The right-rotated configuration (R15) yields similar results, with slopes of 0.315 and 0.408μm/mm and dispersions 0.030 and 0.031 for Days B_1 and B_2, respectively. The left-rotated case (L15) exhibits slightly higher variability, with $\sigma_{r_0}/w_0 = 0.0477$ on Day B_1 (borderline acceptable) and 0.0269 on Day B_2, mainly due to an endpoint deviation at the largest z position. Excluding this isolated outlier restores the fit linearity to $R^2 > 0.9$ and places the data well within the defined alignment tolerances.

In Figure 8.6b, the beam-radius evolution for the reference and the $\pm 15^\circ$ rotations is shown for two separate measurement days on the baseline platform. In all cases, $w(z)$ exhibits a smooth, nearly linear increase along the propagation axis, consistent with the expected diffraction-driven broadening of a Gaussian beam near the waist region. The agreement between days is excellent: the curves overlap within the standard-deviation bars across the entire range, with day-to-day mean differences of 1.9 –2.5μm ($< 1\%$ of w_0). The fitted slopes remain stable between sessions, ranging from 0.10 to $0.12\mu m/mm$ for all conditions, and the determination coefficients exceed $R^2 > 0.96$ except for the left-rotated case on Day 1, which includes a single endpoint deviation around $z = 90$ mm. This isolated excursion slightly increases the apparent slope and inflates the local error bars, but its effect on the mean and overall linearity remains negligible. The behavior reproduces the same pattern observed in the cross-platform comparison, confirming that $w(z)$ is the most stable and geometry-insensitive parameter of the three fitted coefficients. Overall, the day-to-day repeatability of $w(z)$ indicates that both the laser and detection system remain highly stable under the current acquisition protocol, and that minor environmental or mechanical variations between sessions contribute less than 1% to the measured beam-radius evolution.

In Figure 8.6c, P_0 exhibits the largest variability among the fitted parameters. The mean inter-day differences remain small in absolute magnitude (-14.5μW for Refs, -6.6μW for R15, and $+0.19\mu$W for L15), corresponding to less than 1% of the average power. However, the day-to-day root-mean-square deviations reach up to 14.6μW, and the coefficients of variation (CV) differ widely between sessions. For instance, L15 shows a CV of 56.6% on Day 1 versus only 8.8% on Day 2, reflecting the influence of transient fluctuations and the sensitivity of P_0 to small mechanical or alignment perturbations. These oscillations do not correlate with the beam-centering (r_0) or beam-radius (w) metrics, confirming that P_0 is dominated by geometry-dependent interception effects rather than by optical misalignment. In particular, the amplitude of $P_0(z)$ fluctuations is consistent with slight variations in the effective coupling between the partially blocked beam and the detector's active area. Consequently, $P_0(z)$ serves as a secondary consistency indicator, useful for verifying acquisition stability but not suitable for quantitative alignment assessment.

Across the tested rotations, $w(z)$ exhibits sub-percent differences and high linearity, with the only visible deviation attributable to a single endpoint outlier. The center coordinate $r_0(z)$ remains within the "acceptable" dispersion band ($\sigma_{r_0}/w_0 < 0.05$). Table 8.4 summarizes the reproducibility metrics obtained on the baseline platform for the reference and $\pm 15^\circ$ rotated knife configurations. For each pair of days (B_1, B_2), the table lists the linear slopes $|dr_0/dz|$, the normalized dispersion σ_{r_0}/w_0, and the coefficient of

determination R^2 for the beam-center fits, together with the mean absolute error (MAE) and linear trends of $w(z)$ and the corresponding power metrics. The reference condition exhibits the most stable behavior, with $|dr_0/dz| = 0.469$ and 0.496μm/mm and $\sigma_{r_0}/w_0 = 0.021$ and 0.023 for Days B_1 and B_2, respectively. These values fall well within the "acceptable" alignment range defined in Section 8.1. The right-rotated configuration ($R15$) shows similar reproducibility, with slopes of 0.315 and 0.408μm/mm and normalized dispersions of 0.029–0.031. The left-rotated case ($L15$) presents a larger day-to-day shift ($\Delta\overline{w} = 19.6\mu$m, $\approx 4.9\%$), driven by a single endpoint deviation in Day B_1; once this outlier is removed, both the slope (0.113μm/mm) and the dispersion ($\sigma_{r_0}/w_0 = 0.027$) fall inside the nominal alignment tolerances. For the beam radius $w(z)$, the day-to-day differences are minimal: the reference and $R15$ cases differ by only 1.9–2.5μm (below 0.6% of w_0), while $L15$ shows a larger but still controlled variation. In all cases, the fitted slopes ($dw/dz \approx 0.10$–0.12μm/mm) and high linearity ($R^2 > 0.97$) confirm that the local diffraction-driven broadening is consistently reproduced. The retrieved maximum power $P_0(z)$ remains stable within $\pm 15\mu$W, corresponding to $\sim 1\%$ of the mean power, and coefficients of variation below 0.1%.

These results demonstrate that the knife-edge system maintains alignment and measurement stability across different acquisition days. The residual differences in $r_0(z)$ are dominated by reproducible mechanical curvature of the translation stage rather than by true optical drift, confirming the robustness of the automated acquisition scheme.

TABLE 8.4: Day-to-day reproducibility metrics for the baseline platform. Reported parameters include the linear slope $|dr_0/dz|$, normalized dispersion σ_{r_0}/w_0, coefficient of determination R^2, and beam-radius and power metrics. Units: μm/mm for slopes, μm for differences, and μW for power.

Pair	K	$\lvert dr_0/dz\rvert$ [μm/mm]		σ_{r_0}/w_0		$R^2_{r_0}$		$\overline{\Delta w}$	dw/dz	R^2_w
		Day B_1	Day B_2	Day B_1	Day B_2	Day B_1	Day B_2	[μm]	[μm/mm]	
Refs	10	0.469	0.496	0.021	0.023	0.738	0.723	1.95	0.118 / 0.102	0.977 / 0.973
R15	11	0.315	0.408	0.029	0.030	0.432	0.549	2.46	0.121 / 0.104	0.985 / 0.969
L15	11	0.169	0.378	0.047	0.026	0.079	0.576	19.58	−0.789 / 0.113	0.201 / 0.992

8.2 Beam Misalignment Tests

In this second stage of the methodology, the knife-edge scans were performed with the laser beam intentionally misaligned along different transverse directions (up, down, left, and right). Measurements were carried out using two independent translation platforms the baseline and the validation to evaluate the sensitivity of the method to mechanical alignment and platform geometry. The extracted beam parameters were averaged across repetitions, and the corresponding dispersion is represented as error bars.

The results show that the beam-center coordinate $r_0(z)$ is the most sensitive parameter to misalignment. In the vertical configurations particularly *Up* and *Down* $r_0(z)$ exhibits systematic drifts up to approximately 2.5 mm across the scanned range, with slopes between 0.25 µm/mm and 0.40 µm/mm, consistent with small angular deviations of the translation stage or a mechanical tilt of the knife edge. The validation

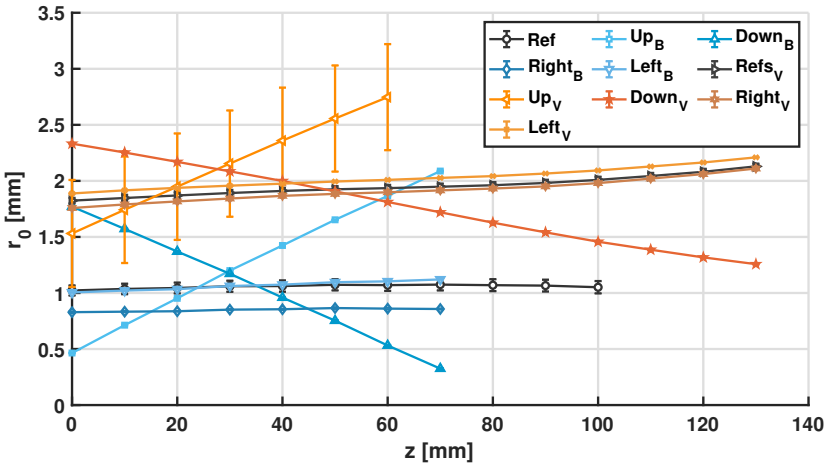

(A) Beam center $r_0(z)$ under different misalignment conditions.

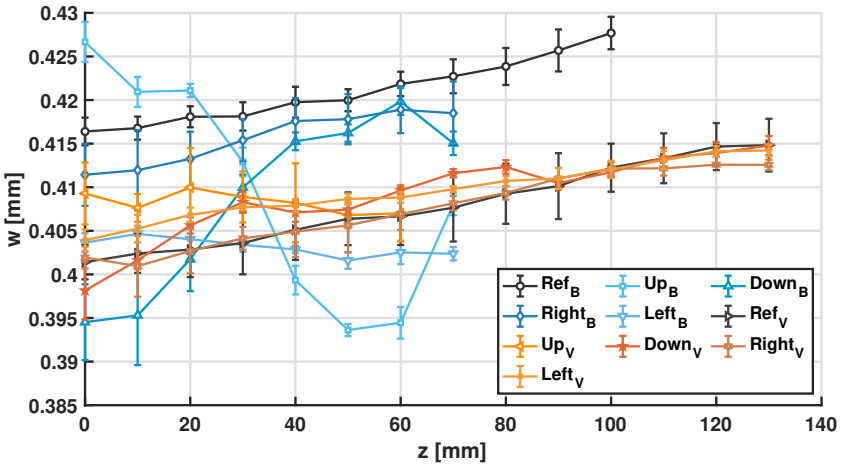

(B) Beam radius $w(z)$ retrieved from knife-edge fits.

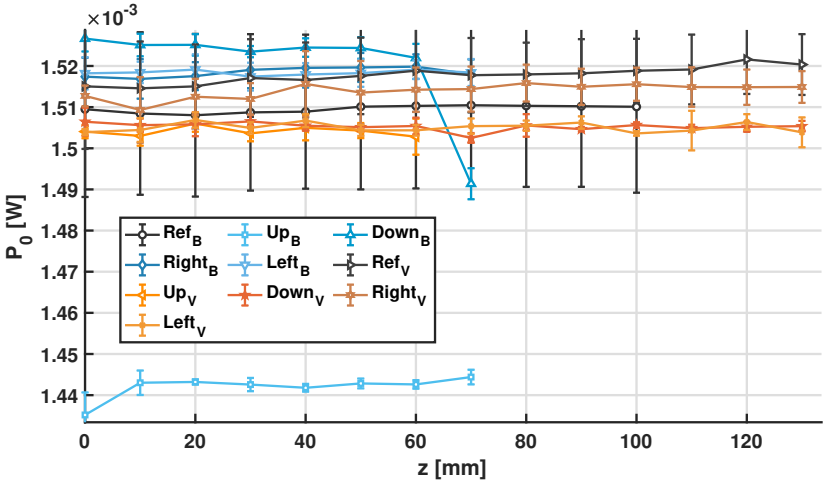

(C) Maximum transmitted power $P_0(z)$ as a function of z.

FIGURE 8.7: Evolution of (a) beam center $r_0(z)$, (b) beam radius $w(z)$, and (c) transmitted power $P_0(z)$ under misalignment conditions.

platform displays the same qualitative behavior but with larger offsets, revealing the influence of its intrinsic curvature on the beam center trajectory. In contrast, the beam radius $w(z)$ remains stable across all configurations, with mean values around 0.41 mm and slopes below 0.15 µm/mm. The dispersion between conditions does not exceed 2%, confirming that the waist estimation is largely unaffected by moderate mechanical or alignment perturbations. This finding validates the robustness of the knife-edge reconstruction for retrieving the beam width, even under small angular deviations. The transmitted power $P_0(z)$ shows only minor fluctuations, with differences below 20 µW relative to the reference (less than 1.5% of the mean power). The lack of correlation between $P_0(z)$ and $r_0(z)$ confirms that the drifts observed in r_0 arise from geometric factors such as stage curvature or knife tilt rather than from fluctuations in the laser output. It is important to note that, for the upward misalignment case on the validation platform, only the first seven data points are shown. During acquisition, as the knife edge moved farther from the beam aperture, the transmission curves progressively shifted toward higher positions until the knife could no longer intercept the entire beam. Beyond this range, the signal became dominated by noise, causing the fit to fail. This effect is illustrated in Figure 8.8, which shows the raw error function curves $erf(x)$ corresponding to successive axial positions z. The rightward displacement of the profiles clearly reveals the gradual loss of overlap between the knife and the beam.

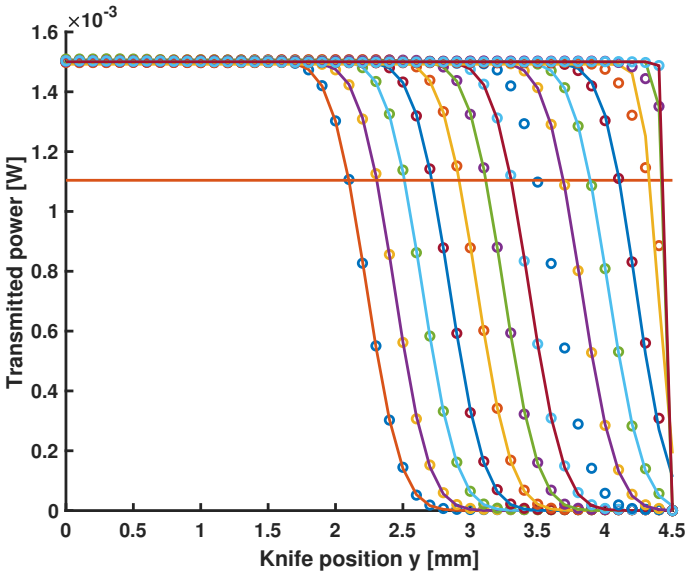

FIGURE 8.8: Upward misalignment case on the validation platform. The sequence of transmission curves $erf(x)$ progressively shifts toward higher knife positions as the beam aperture moves away from the blade, until the knife can no longer block the beam. Beyond this range, the signal becomes dominated by noise, resulting in non-convergent fits (the nearly flat curve on the right). Only the stable portion of the data (first seven points) was included in the analysis.

The truncated portion corresponds to the stable regime that accurately represents the beam-center behavior under this condition. This observation motivated the implementation of smaller upward and downward displacements in subsequent alignment

tests, ensuring that the full beam profile remained within the measurable range while preserving sensitivity to small angular deviations. $r_0(z)$ serves as a sensitive indicator of mechanical and geometrical distortions, while $w(z)$ and $P_0(z)$ remain largely unaffected. The following section focuses exclusively on the baseline platform, analyzing its mechanical behavior in greater detail to assess reproducibility and long-term alignment stability. Thus the knife-edge technique provides a clear and quantitative diagnostic of beam misalignment.

8.2.1 Baseline Platform under Deliberate Misalignment

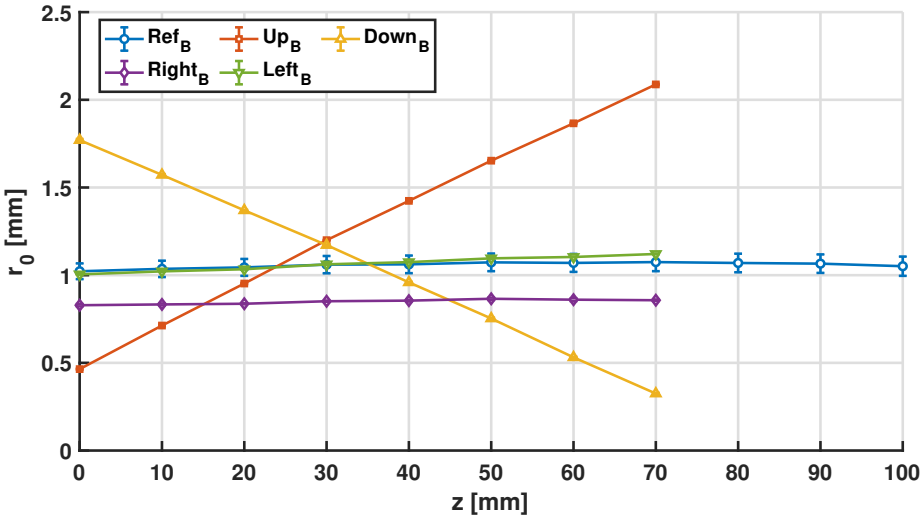

FIGURE 8.9: Baseline platform: beam center $r_0(z)$ (mean $\pm$ SD) under Up/Down/Left/Right misalignment.

Misalignment manifests primarily as a direction dependent drift of the beam center trace. The *Up* case shows a strong positive slope, with r_0 increasing from approximately 0.5 mm to 2.1 mm over the 70 mm scanned range, corresponding to a slope of about 0.40µm/mm. Conversely, *Down* displays a nearly symmetric negative trend of comparable magnitude ($-0.38 m/mm$), while *Left* and *Right* exhibit small drifts ($< 0.10 m/mm$) that remain within the alignment bounds defined in Section 8.1. The reference trace remains stable around $r_0 \approx 1.0$ mm with dispersion below 0.02 mm, confirming high repeatability under aligned conditions. The low spread of all traces indicates that these trends are geometric rather than stochastic consistent with a rigid body tilt of the optical axis relative to the stage motion. In this context, the sign of dr_0/dz encodes the misalignment direction, whereas the magnitude of $|dr_0/dz|$ acts as a scalar indicator of its severity.

The beam radius $w(z)$ remains comparatively stable across all configurations. Mean values cluster around 0.41 mm with standard deviations below 0.005 mm, representing less than 2% relative variation. Relative to the reference, *Left* and *Right* remain nearly indistinguishable, whereas *Up* and *Down* exhibit mild deviations (up to $\pm$0.01 mm) near intermediate z positions. These small variations confirm that the beam size estimation is

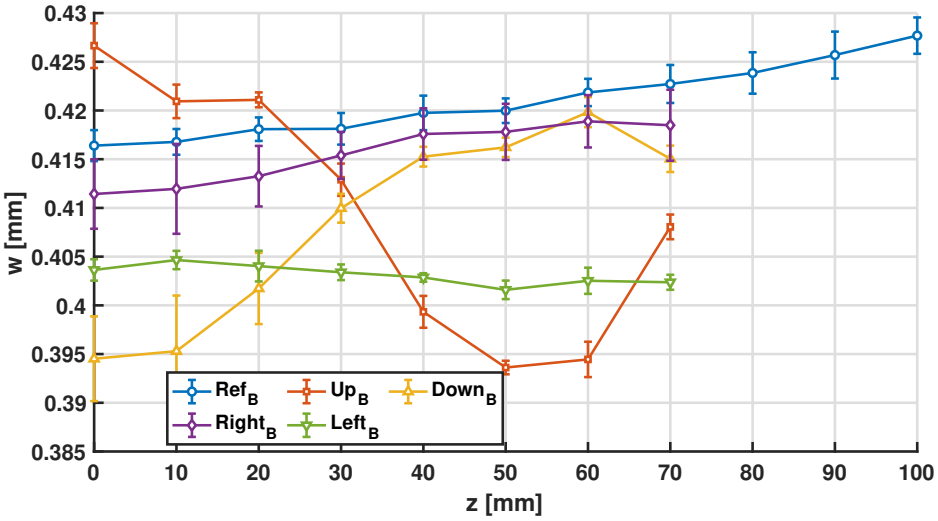

FIGURE 8.10: Baseline platform: beam radius $w(z)$ (mean $\pm$ SD).

much less sensitive to alignment perturbations than $r_0(z)$, implying that misalignment primarily affects the beam footprint rather than its waist.

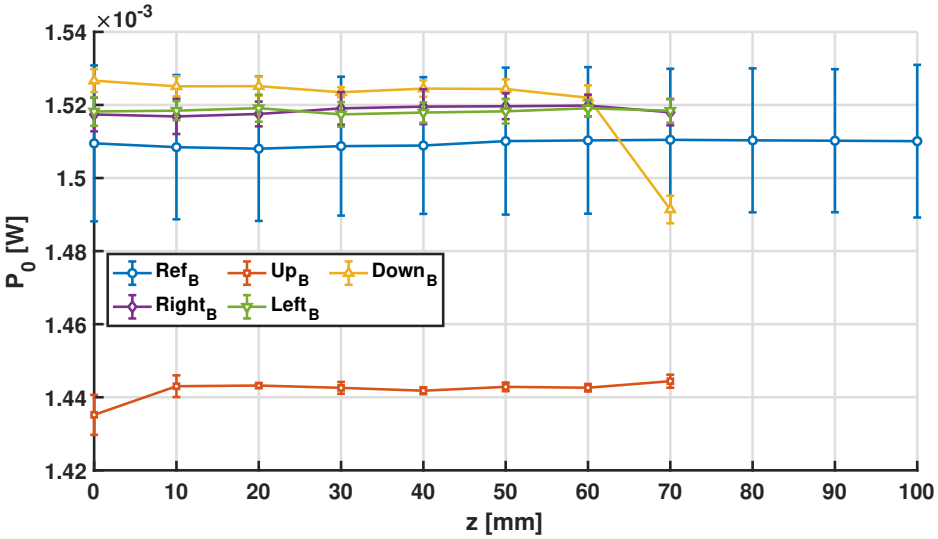

FIGURE 8.11: Baseline platform: maximum power $P_0(z)$ (mean $\pm$ SD).

The maximum transmitted power $P_0(z)$ exhibits direction-dependent DC offsets with weak axial dependence. *Down* consistently yields higher P_0 values (1.523 mW) than the reference (1.510mW), while *Up* remains below it (1.44 mW). Lateral displacements (*Left*/*Right*) follow the reference closely, with mean differences smaller than 0.01 mW ($<$ 1%). Because these offsets originate from partial beam interception and detector coupling geometry rather than optical misalignment, $P_0(z)$ is used here only as a qualitative stability indicator.

On the baseline platform, deliberate misalignment is most robustly detected by the pair $\{\, \sigma_{r_0}/w_0,\ |dr_0/dz| \,\}$. The first quantifies repeatability, while the second provides a

monotonic indicator whose sign reveals the misalignment direction. The beam radius $w(z)$ acts as a passive stability sentinel, its bounded variations confirm that the optical waist remains well characterized, whereas $P_0(z)$ captures alignment dependent offsets without diagnostic significance. These results validate the use of $r_0(z)$-based metrics as the primary figures of merit for assessing alignment quality and stage reproducibility.

8.3 Beam Waist Estimation

This section presents the final stage of the knife-edge analysis, where the alignment metrics developed in the previous chapters were applied to evaluate the behavior of the parameters r_0, w, and P_0 during the beam waist estimation process. The goal of this stage was to verify how these parameters evolve when the focusing lens is introduced and to assess the stability of the measurement. A total of nineteen reference measurements were acquired over two different days under nearly identical conditions, without the focusing lens. In these measurements, the distance between the initial knife-edge position and the detector was approximately 25 cm, while the distance from the laser aperture to the knife-edge varied slightly between runs. The transverse step size for the knife-edge movement was fixed at 0.1 mm. In contrast, seventeen additional measurements were performed with the focusing lens inserted, also over two days and under comparable conditions. In this case, the transverse step size ranged between 0.05 and 0.03 mm to ensure higher resolution near the focal region. The figures presented in this section display the averaged curves for each parameter along with their corresponding dispersion, represented as uncertainty bands. Before proceeding with the waist estimation, it is worth recalling some of the observations made in the previous sections. When the knife-edge was rotated and the laser misaligned, it was possible to determine how sensitive the fitted parameters: r_0, w, and P_0 are to imperfections in the blade itself, the component that effectively enables us to 'measure' the light distribution, and that even under substantial deviations, the fitted parameters preserve coherent trends, confirming the robustness of the knife edge method and allowing us to quantify the degree of misalignment through the dispersion and slope metrics (σ_{r_0}/w_0 and $|dr_0/dz|$).

Figure 8.12 summarizes the results obtained from both reference and focused measurements. As in previous sections, the reference measurements were performed over a wide axial range to confirm the proper alignment of the setup. In this case, the scans were taken over 100 mm with a step size of 10 mm in z and a transverse resolution of 0.1 mm for the knife edge movement. The resulting $r_0(z)$ curves (Fig. 8.12a) display consistent slopes across all reference datasets, confirming the mechanical repeatability of the translation stage. In contrast, the waist measurements performed with the focusing lens covered a much shorter axial range between 25 and 40 mm, with step sizes of 3 and 5 mm in z. This higher sampling density was required because the beam radius decreased by nearly an order of magnitude, demanding finer resolution near the focal region. As expected, the $r_0(z)$ curves in these cases are shorter but denser, corresponding to the region of highest optical convergence.The beam radius $w(z)$ (middle panel in Fig. 8.12) confirms this behavior. The beam diverges progressively after the focal region, reaching values close to 0.43 mm. The difference between the curves obtained with and without the focusing lens is clearly visible, as is the disparity in scan range and resolution.

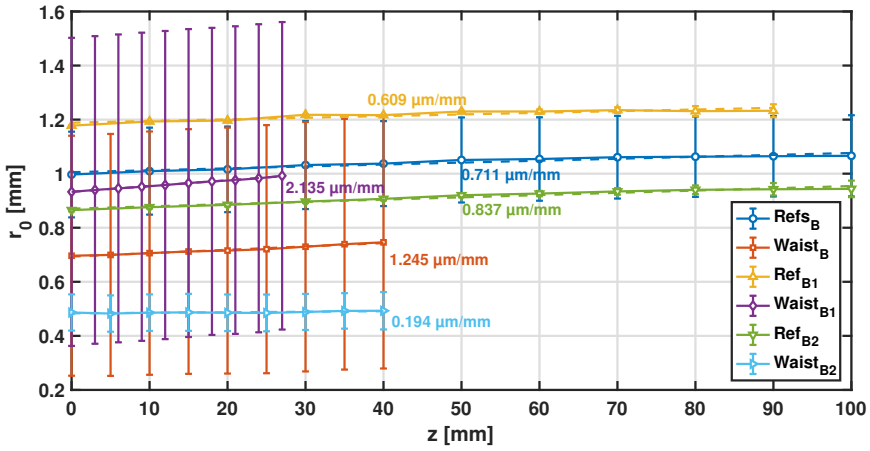

(A) $r_0(z)$ trends for reference and waist datasets.

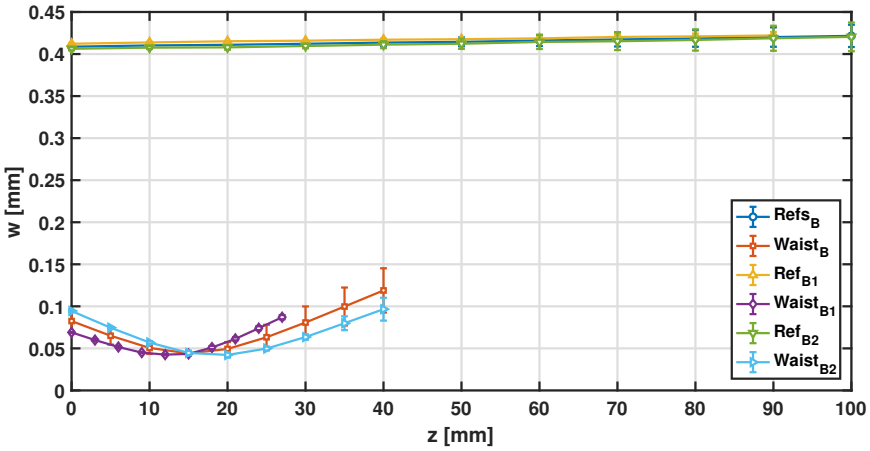

(B) Beam radius $w(z)$ for all measurement sets.

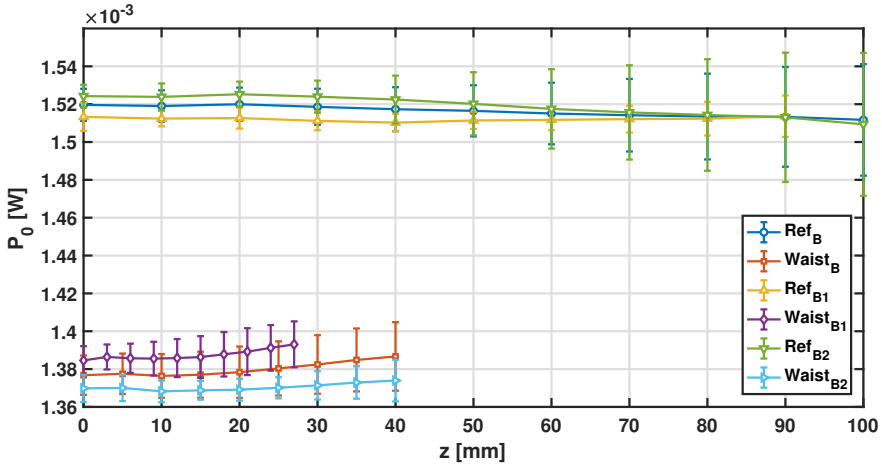

(C) Peak power $P_0(z)$ showing lens-induced transmission loss.

FIGURE 8.12: Experimental results for beam-waist estimation from knife-edge analysis. The panels show the evolution of r_0, w, and P_0 along z for reference and waist datasets acquired with and without the focusing lens.

From this graph, the beam waist can already be estimated to be around 0.05 mm, indicating that the beam is compressed by approximately one order of magnitude compared to the unfocused configuration. The maximum transmitted power $P_0(z)$ (bottom panel in Fig. 8.12) behaves similarly to $w(z)$ but exhibits slight decay trends. For the reference measurements, a small decrease in power is observed along z, possibly caused by minor curvature of the translation stage or slow fluctuations in the laser output. When the lens is introduced, the decay becomes more evident (approximately 0.1 mW difference), together with a slight increase in uncertainty. These effects are likely due to reflection losses and small misalignments induced by the lens, yet the power remains stable enough to preserve measurement reliability.

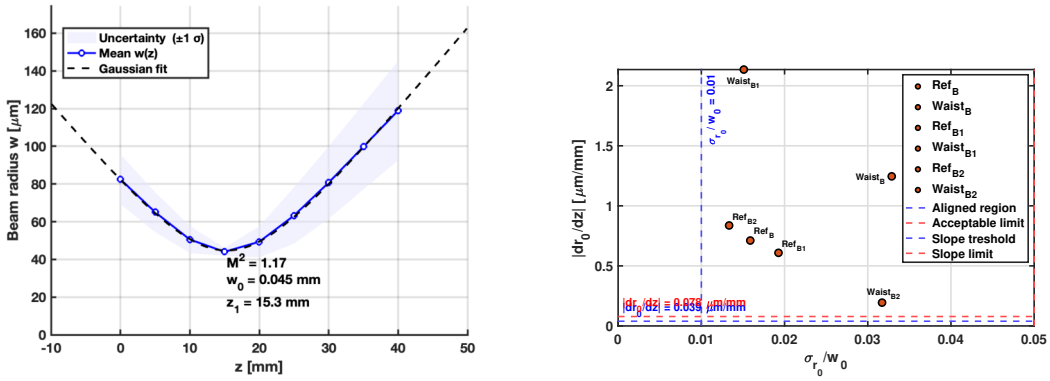

(A) Gaussian beam waist characterization (mean ± std).

(B) Alignment stability map for beam-waist datasets.

FIGURE 8.13: (a) Gaussian fit to the mean beam radius data showing a waist of $w_0 = 45\mu$m and $M^2 = 1.17$. (b) Alignment map comparing beam stability metrics across measurement sets.

The final two plots in Figure 8.13 summarize the overall waist characterization and alignment evaluation. The left panel shows the Gaussian propagation fit applied to the averaged waist data, yielding $w_0 = 45\mu$m, $z_R = 15.3$ mm, and a beam quality factor $M^2 = 1.17$. These values confirm a nearly diffraction-limited behavior. The right panel presents the alignment stability map derived from the metrics σ_{r_0}/w_0 and $|dr_0/dz|$, using tolerance limits of 0.039 and 0.078 μm/mm, which correspond to displacements of 0.25 and 0.5 w_0 over the full 255 mm scan range. According to these theoretical thresholds, none of the datasets strictly fall within the "ideal" alignment range; however, all remain within the region of acceptable alignment. This confirms that even with a systematic curvature of approximately 0.8 μm/mm—an intrinsic mechanical signature of the translation system—the beam waist estimation remains consistent, and the knife-edge method continues to perform reliably.

The consistency between datasets confirms the reproducibility of the measurements, while the combination of alignment and beam-waist metrics provides a comprehensive and quantitative framework for evaluating alignment quality in focused optical configurations. In nonlinear optics, such precision in waist estimation is particularly relevant, since the local intensity and therefore the nonlinear response of the medium depends critically on the beam waist. Accurate characterization of w_0 ensures that the measured

nonlinear refractive index and susceptibility values are not affected by geometric artifacts, thus establishing a reliable foundation for subsequent Z scan and other nonlinear optical experiments. In nonlinear optics, such precision in waist estimation is particularly relevant, since the local intensity and therefore the nonlinear response of the medium depends critically on the beam waist. Accurate characterization of w_0 ensures that the measured nonlinear refractive index and susceptibility values are not affected by geometric artifacts, thus establishing a reliable foundation for subsequent Z scan and other nonlinear optical experiments.

8.4 Materials Tested and Absence of Nonlinear Response

A key objective of this work was to experimentally determine the nonlinear refractive index n_2 of candidate materials using the Z-scan technique. However, no reproducible nonlinear signal was detected in any of the available samples, including $BaTiO_3$, SBN:61 ($Sr_{0.61}Ba_{0.39}Nb_2O_6$), and homemade hibiscus-based organic films. This section reviews the attempted experiments, probable causes of failure, and critical limitations in the material selection and laboratory process. The $BaTiO_3$ sample was an undoped, 2 mm thick bulk crystal with unknown fabrication parameters. Despite multiple Z-scan trials under varying step sizes and scan ranges, no peak–valley structure or any detectable change in transmission was observed. This outcome is consistent with previous literature reporting that undoped $BaTiO_3$ crystals exhibit negligible third-order optical nonlinearity under continuous wave (CW) illumination [41]. Most significant nonlinear responses in $BaTiO_3$ have been demonstrated in thin films or nanoparticles, especially when doped with elements such as Fe, Rh, or Au, and under femtosecond or nanosecond pulse excitation. Reported values of n_2 in such doped structures range from 10^{-13} to $10^{-15}\,m^2/W$, often accompanied by strong RSA (reverse saturable absorption) or TPA (two-photon absorption) signals [41], [42], [43], [44]. These effects are highly sensitive to preparation methods, such as pulsed laser deposition, sol-gel processing, or chemical doping, as well as to the crystallinity, morphology, and carrier density of the sample. In our case, the excitation wavelength (543.5 nm) is comparable to those used in prior works, but the low incident power ($\sim$1.5 mW) and CW regime fall outside the typical excitation conditions required to observe significant nonlinear optical responses. Furthermore, the millimeter-scale thickness of the sample reduces the effective nonlinear phase shift due to diffraction and absorption losses. These factors, combined with the unknown quality and composition of the crystal, likely explain the absence of any observable third-order effects.

The second sample tested was a 5 mm thick SBN:61 ($Sr_{0.61}Ba_{0.39}Nb_2O_6$) crystal, a well-known photorefractive ferroelectric belonging to the tungsten–bronze family. Although SBN materials can exhibit large electro-optic and photorefractive coefficients, their third-order susceptibility $\chi^{(3)}$ under continuous-wave excitation is typically weak unless strong charge-transport mechanisms or high-intensity ultrafast pulses are involved. Previous studies have reported significant enhancements of $\chi^{(3)}$ in SBN only under picosecond or femtosecond excitation, or in thin-film geometries where defect-mediated charge-transfer states dominate the nonlinear response [45], [46], [47], [48]. Conversely, bulk SBN crystals under low-power CW illumination show very small nonlinear refractive index values, often below 10^{-15}–$10^{-16}\,m^2/W$, making Z-scan detection extremely challenging [49], [50]. In our configuration, the incident power and beam

waist yield intensities that are orders of magnitude below those typically required to activate photorefractive space-charge fields or carrier-driven nonlinear refraction in SBN. Furthermore, the crystal thickness introduces strong diffraction and walk-off effects that dilute any small nonlinear phase shift. No peak–valley signature was observed in the closed-aperture Z-scan, and the open-aperture signal remained flat across all positions, consistent with a purely linear response. Under the low-intensity CW regime used here, the material, thickness, and excitation conditions were insufficient to generate any detectable nonlinear refractive or absorptive effects.

A set of homemade gelatin-based films incorporating *Hibiscus sabdariffa* extract were also tested. These samples were physically inconsistent, with variable thickness and optical density. Only one measurement showed a weak peak–valley structure, which could not be replicated. Prior research using femtosecond pulses has shown transient nonlinear absorption and optical limiting in hibiscus extracts [51], [52], but these effects are not expected under low-intensity CW excitation.

Overall, the experimental phase was hindered by poor coordination, and the absence of robust sample characterization. None of the materials were provided with datasheets or verified optical properties. Critical experimental parameters, such as beam waist–sample thickness matching, spatial homogeneity, and thermal stability, were not controlled. These shortcomings made it impossible to isolate or confirm third-order nonlinear effects. This experience highlights the importance of experimental rigor and interdisciplinary planning. Even well-established techniques such as Z-scan require strict control of beam parameters, sample quality, and detection sensitivity. Future work must prioritize traceable sample acquisition, validation of optical properties prior to testing, and adequate power levels matched to the nonlinear thresholds of the materials.

Chapter 9

Conclusion

This thesis presented the development and validation of an automated experimental and computational framework for the precise characterization of laser beams using the knife-edge technique. The system was conceived as a foundational tool for nonlinear optical measurements, where the accuracy of the beam waist directly determines the reliability of derived quantities such as the nonlinear refractive index n_2 and the third-order susceptibility $\chi^{(3)}$. From a theoretical perspective, the work established a consistent formulation linking the Gaussian beam model, the knife-edge power transmission function, and the beam propagation law. The nonlinear least-squares fitting procedure implemented in MATLAB was described in detail, including its parameterization, initialization, and robust weighting strategy. Furthermore, an alignment analysis based on the beam-center evolution $r_0(z)$ was introduced, providing quantitative metrics to assess the mechanical stability and optical alignment of the setup. Experimentally, the integration of automated motion control, optical power acquisition, and data processing allowed the reconstruction of complete beam profiles with minimal human intervention. The two-step fitting procedure, transverse scans followed by axial propagation analysis, yielded consistent estimates of the beam waist w_0, waist position z_0, and Rayleigh range z_R, demonstrating both repeatability and physical coherence across multiple datasets. In the context of nonlinear optics, the study underscored the fundamental role of accurate beam waist determination in the quantification of intensity-dependent refractive index changes. Since $I_0 = 2P_0/(\pi w_0^2)$, even small uncertainties in w_0 can significantly affect the calculated values of n_2 and $\chi^{(3)}$. The automated system developed here provides a reliable solution to this problem, establishing a reproducible methodology for experimental studies involving nonlinear refractive effects, Z-scan characterization, and other intensity-dependent phenomena.

In summary:

1. The formulation of a unified theoretical and numerical model for knife-edge data fitting and propagation analysis.

2. The implementation of an automated experimental platform integrating motion control, sensing, and data processing.

3. The demonstration of the relevance of accurate beam profiling for the quantification of nonlinear optical parameters.

Beyond its immediate application, this work provides a general framework adaptable to other beam diagnostic or characterization tasks in photonics. Future efforts may include extending the system to measure multimode or non-Gaussian beams or directly

coupling the beam characterization module with Z-scan measurements. Such developments would further strengthen the link between optical instrumentation and the precise determination of nonlinear optical properties. The value of this work lies in establishing a reliable metrological foundation for experiments in which beam characterization is not a peripheral task but a determining factor in the interpretability of the results. By consolidating automation, robust fitting, and alignment diagnostics into a single framework, this thesis equips future nonlinear-optics measurements with the level of beam control they require to be meaningful. With the characterization method now in place, the next steps focus on applying it under conditions where nonlinear effects can actually emerge. When those experiments are carried out, they will rely on a beam measurement procedure that is already validated and ready to support more demanding optical studies.

Bibliography

[1] B. E. A. Saleh and M. C. Teich, *Fundamentals of Photonics*, 3rd. John Wiley & Sons, 2019, ISBN: 978-1119506874.

[2] A. E. Siegman, *Lasers*. Mill Valley, California: University Science Books, 1986, 1283 pp., Literaturangaben, ISBN: 978-0935702118.

[3] E.-G. Neumann, "Gaussian beams", in *Single-Mode Fibers: Fundamentals*. Berlin, Heidelberg: Springer Berlin Heidelberg, 1988, pp. 35–60, ISBN: 978-3-540-48173-7. DOI: 10.1007/978-3-540-48173-7_4. [Online]. Available: https://doi.org/10.1007/978-3-540-48173-7_4.

[4] H. Kogelnik and T. Li, "Laser beams and resonators", *Applied Optics*, vol. 5, no. 10, pp. 1550–1567, 1966. DOI: 10.1364/AO.5.001550.

[5] G. Goubau and F. Schwering, "On the guided propagation of electromagnetic wave beams", *IRE Transactions on Antennas and Propagation*, vol. 9, no. 3, pp. 248–256, 1961. DOI: 10.1109/TAP.1961.1144994. [Online]. Available: https://ieeexplore.ieee.org/abstract/document/1144999.

[6] A. V. Popov, "Gaussian beam propagation and focusing of laser radiation", *Soviet Journal of Quantum Electronics*, vol. 12, no. 10, pp. 1365–1370, 1982, Original article; DOI resolver inactive or unavailable.

[7] A. A. Bogush and V. A. Shramkova, "Investigation of laser beam profiles in nonlinear optical media", *Optics and Spectroscopy*, vol. 61, no. 2, pp. 236–239, 1986, Translated from *Optika i Spektroskopiya*.

[8] R. Menzel, *Photonics: Linear and Nonlinear Interactions of Laser Light and Matter*. Springer, 2007, ISBN: 978-3540721911.

[9] R. W. Boyd, *Nonlinear Optics*, 3rd. San Diego: Academic Press, 2008, ISBN: 978-0-12-369470-6.

[10] Y. Suzaki and A. Tachibana, "Measurement of the μm sized radius of Gaussian laser beam using the scanning knife-edge", *Appl. Opt.*, vol. 14, no. 12, pp. 2809–2810, 1975. DOI: 10.1364/AO.14.002809. [Online]. Available: https://opg.optica.org/ao/abstract.cfm?URI=ao-14-12-2809.

[11] H. R. Bilger and T. Habib, "Knife-edge scanning of an astigmatic Gaussian beam", *Applied Optics*, vol. 24, no. 5, pp. 686–690, 1985. DOI: 10.1364/AO.24.000686.

[12] J. M. Khosrofian and B. A. Garetz, "Measurement of a Gaussian laser beam diameter through the direct inversion of knife-edge data", *Applied Optics*, vol. 22, no. 21, pp. 3406–3410, 1983. DOI: 10.1364/AO.22.003406.

[13] M. A. C. de Araújo, R. Silva, E. de Lima, D. P. Pereira, and P. D. de Oliveira, "Measurement of Gaussian laser beam radius using the knife-edge technique: Improvement on data analysis", *Applied Optics*, vol. 48, no. 2, pp. 393–396, 2009. DOI: 10.1364/AO.48.000393.

[14] K. Purvis, R. Cisek, and D. Tokarz, "New activity for instrumental analysis: Laser beam profiling", *Journal of Chemical Education*, vol. 96, no. 9, pp. 1977–1981, 2019. DOI: 10.1021/acs.jchemed.9b00484.

[15] A. B. Ortega, M. L. A. Carrasco, J. A. D. Pintle, M. M. M. Otero, and M. D. I. Castillo, "New method to characterize Gaussian beams", in *22nd Congress of the International Commission for Optics: Light for the Development of the World*, International Society for Optics and Photonics, vol. 8011, SPIE, 2011, p. 80114X. DOI: 10.1117/12.902192. [Online]. Available: https://doi.org/10.1117/12.902192.

[16] T. Szirányi, P. Barczikay, and T. Kovács, "Measurement of laser-beam-diameter of some μm by moving ccd sensor", in *Laser/Optoelektronik in der Technik / Laser/Optoelectronics in Engineering*, W. Waidelich, Ed., Springer Berlin Heidelberg, 1987, pp. 374–378, ISBN: 978-3-642-83174-4.

[17] R. Díaz-Uribe, M. Rosete-Aguilar, and R. Ortega-Martínez, "Position sensing of a Gaussian beam with a power meter and a knife edge", *Revista Mexicana de Física*, vol. 39, pp. 484–492, 1992.

[18] M. M. M. Rashad, "Measurements of laser beam using knife edge technique", 2019.

[19] D. Wright, P. Greve, J. Fleischer, and L. Austin, "Laser beam width, divergence and beam propagation factor – an international standardization approach", *Optics & Quantum Electronics*, vol. 24, S993–S1000, 1992.

[20] J. Arnaud, W. Hubbard, G. Mandeville, B. de la Clavière, E. Franke, and J. Franke, "Technique for fast measurement of Gaussian laser beam parameters", *Applied Optics*, vol. 10, no. 12, pp. 2775–2776, 1971. DOI: 10.1364/AO.10.002775.

[21] R. L. McCally, "Measurement of Gaussian beam parameters", *Applied Optics*, vol. 23, no. 14, p. 2227, 1984. DOI: 10.1364/AO.23.002227.

[22] M. González-Cardel, P. Arguijo, and R. Díaz-Uribe, "Gaussian beam radius measurement with a knife-edge: A polynomial approximation to the inverse error function", *Applied Optics*, vol. 52, no. 16, pp. 3849–3855, 2013. DOI: 10.1364/AO.52.003849.

[23] S. Nemoto, "Determination of waist parameters of a Gaussian beam", *Applied Optics*, vol. 25, pp. 3859–3863, 1986.

[24] W. Plass, R. Maestle, K. Wittig, A. Voss, and A. Giesen, "High-resolution knife-edge laser beam profiling", *Optics Communications*, vol. 134, no. 1, pp. 21–24, 1997, ISSN: 0030-4018. DOI: https://doi.org/10.1016/S0030-4018(96)00527-5. [Online]. Available: https://www.sciencedirect.com/science/article/pii/S0030401896005275.

[25] J. A. Arnaud, *Beam and fiber optics*. Elsevier, 2012.

[26] *Lasers and laser-related equipment — test methods for laser beam widths, divergence angles and beam propagation ratios — part 1: Stigmatic and simple astigmatic beams*, Supersedes ISO 11146-1:2005, Geneva, Switzerland, 2021.

[27] Thorlabs GmbH, "PM100D optical power and energy meter", Dachau, Germany, Tech. Rep., 2023, Operation Manual, Version 17654-D02 REVJ. [Online]. Available: https://www.thorlabs.com.

[28] S. C. Chapra and R. P. Canale, *Numerical Methods for Engineers*, 8th. McGraw-Hill Education, 2020.

[29] P. R. Bevington and D. K. Robinson, *Data Reduction and Error Analysis for the Physical Sciences*, 3rd. McGraw-Hill, 2003.

[30] G. A. F. Seber and C. J. Wild, *Nonlinear Regression*. Wiley-Interscience, 2003.

[31] W. H. Press, S. A. Teukolsky, W. T. Vetterling, and B. P. Flannery, *Numerical Recipes: The Art of Scientific Computing*, 3rd. Cambridge University Press, 2007.

[32] I. The MathWorks, *Fitnlm - nonlinear regression model*, https://www.mathworks.com/help/stats/fitnlm.html, 2024.

[33] I. The MathWorks, *Robust regression using bisquare and huber weighting*, https://www.mathworks.com/help/stats/robust-regression.html, 2024.

[34] R. W. Boyd, *Nonlinear Optics*, 4th. Academic Press, 2020, ISBN: 978-0-12-811002-7. DOI: 10.1016/C2015-0-05510-1. [Online]. Available: https://www.sciencedirect.com/book/9780128110027/nonlinear-optics.

[35] P. E. Powers, *Fundamentals of Nonlinear Optics*. CRC Press, 2017, ISBN: 9780429193255. DOI: 10.1201/b12037. [Online]. Available: https://www.taylorfrancis.com/books/mono/10.1201/b12037/fundamentals-nonlinear-optics-peter-powers.

[36] M. Sheik-Bahae, A. A. Said, T.-H. Wei, D. J. Hagan, and E. W. Van Stryland, "Sensitive measurement of optical nonlinearities using a single beam", *IEEE Journal of Quantum Electronics*, vol. 26, no. 4, pp. 760–769, 1990.

[37] M. Sheik-Bahae and E. W. Van Stryland, *Z-scan measurements of optical nonlinearities*, CREOL, University of Central Florida, Technical Report, 1999.

[38] *Lasers and laser-related equipment — test methods for laser-induced damage threshold*, Parts 1–4, Geneva, Switzerland: International Organization for Standardization, 2021. [Online]. Available: https://www.iso.org/standard/77769.html.

[39] R. Y. Chiao, E. Garmire, and C. H. Townes, "Self-trapping of optical beams", *Physical Review Letters*, vol. 13, no. 15, pp. 479–482, 1964.

[40] L. Bergé, S. Skupin, R. Nuter, J. Kasparian, and J.-P. Wolf, "Ultrashort filaments of light in weakly ionized, optically transparent media", *Reports on Progress in Physics*, vol. 70, no. 10, p. 1633, 2007.

[41] W. F. Zhang, H. Yu, and S. Zhang, "Nonlinear optical absorption in undoped and Ce-doped $BaTiO_3$ thin films using Z-scan technique", *Applied Physics Letters*, vol. 76, no. 8, pp. 1003–1005, 2000.

[42] G. Yang, Z. Zhou, Y. Liu, and J. Zhang, "Large optical nonlinearities in rh:batio$_3$ thin films prepared by pulsed laser deposition", *Applied Physics Letters*, vol. 80, no. 7, pp. 1193–1195, 2002.

[43] Y. Tian, X. Liu, and L. Wang, "Optical nonlinearities in Fe-doped $BaTiO_3$ thin films prepared by sol–gel method", *Optics Communications*, vol. 366, pp. 320–325, 2016.

[44] A. Y. Fasasi, M. Maaza, and Z. Nuru, "Z-scan characterization of Zn-doped $BaTiO_3$ thin films", *Physica B: Condensed Matter*, vol. 403, no. 1, pp. 118–123, 2008.

[45] H. Liu, "Spectroscopic studies of novel materials for display and nlo applications", Tech. Rep., 2001.

[46] E. Beyreuther et al., "Photoconduction of polar and nonpolar cuts of undoped $sr_{0.61}ba_{0.39}nb_2o_6$ single crystals", *Crystals*, vol. 11, no. 7, p. 780, 2021. DOI: 10.3390/cryst11070780. [Online]. Available: https://www.mdpi.com/2073-4352/11/7/780.

[47] K. S. Chen, H. S. Gu, and W. Q. Cao, "Large third-order optical nonlinearity in Cu-Doped $SrBi_2Nb_2O_9$ thin films", *European Physical Journal Applied Physics*, vol. 40, pp. 65–69, 2007. DOI: 10.1051/epjap:2007122.

[48] A. Ródenas, C. Jacinto, L. R. Freitas, D. Jaque, and T. Catunda, "Nonlinear refraction and absorption through phase transition in a nd:sbn laser crystal", *Phys. Rev. B*, vol. 79, p. 033 108, 3 2009. DOI: 10.1103/PhysRevB.79.033108. [Online]. Available: https://link.aps.org/doi/10.1103/PhysRevB.79.033108.

[49] M. Stepić, "Nonlinear optics in photorefractive crystals: Theory and experiments", Ph.D. dissertation, University of Belgrade, 2002.

[50] I. Biaggio, "Photorefractive and nonlinear optical processes in strontium barium niobate crystals", Ph.D. dissertation, École Polytechnique Fédérale de Lausanne, 2005.

[51] R. Helguera, D. López, and P. González, "Propiedades ópticas no lineales en soluciones de hibiscus sabdariffa usando técnica z-scan", *Revista Mexicana de Física*, vol. 62, pp. 499–508, 2016.

[52] J. López-Sandoval, I. García, and A. Hernández, "Propiedades ópticas no lineales y absorción transitoria en solución colorante hibiscus sabdariffa probadas con pulsos de femtosegundos", *Materiales Ópticos*, vol. 45, pp. 131–139, 2023.